Kinematics of Electroweak Single-Top-Quark Production

Jan Lück

Diploma Thesis

at the Faculty for Physics
of the University of Karlsruhe

Referee: Prof. Dr. Th. Müller
Institut für Experimentelle Kernphysik

Co-Referee: Prof. Dr. M. Feindt
Institut für Experimentelle Kernphysik

January 13, 2006

Introduction

Besides the top quark pair production via the strong interaction, discovered at the Fermilab Tevatron Collider in 1995 by the CDF and DØ collaborations [1, 2], the Standard Model (SM) also predicts the electroweak production of single-top-quarks, which has not yet been observed. The discovery of single-top production and the subsequent precise measurement of its cross section are main goals of the collaborations at the Fermilab Tevatron Collider. In Run I (1992-95) of the Tevatron several upper limits on single-top production cross sections were set by the CDF [3, 4] and DØ [5, 6] experiments. The Run I results have been recently surpassed by the latest Run II measurements [7, 8]. A comprehensive review of top quark physics can be found in reference [9].

A good understanding of the signal characteristics of the relevant single-top production modes is indispensable for further analyses. For the s-channel production mode, the available Monte Carlo (MC) generators are in good agreement with the next-to-leading-order (NLO) calculations. The t-channel production mode has one important NLO contribution which is not modeled by the present leading-order (LO) MC generators. This leads to the fact that there is yet no generator which produces an appropriate signal sample. The Tevatron Run I analyses used the PYTHIA MC generator [10], knowing that it is not accurate in some aspects. As a workaround a matching procedure of two matrix element MC samples was proposed [11] to compensate for the inaccuracy. In the recent Run II single-top analysis the CDF Collaboration used besides the LO sample an additional sample, which models the important NLO contribution. In the following this will be called NLO sample. Both are produced by the MadEvent MC generator [12, 13], showered by PYTHIA and matched in such a way as to achieve an improved modeling [14].

In this thesis, the matching of the t-channel samples is optimized. This is done by comparing the distribution, which has to be matched, to the prediction of a next-to-leading-order calculation, provided by the ZTOP software [15]. The occurring differences are minimized by changing the matching parameters, especially the fraction of the NLO sample. The s- and newly matched t-channel signal samples are then validated by means of the ZTOP NLO calculations. The resulting deviations are used to estimate the systematic uncertainty on the Monte Carlo model.

In the second part of this thesis, a new method of the measurement of the s- and t-channel cross sections is introduced. The MadEvent MC signal samples are thereby used to train two independent neural networks (NN). The output of the networks provide the opportunity to measure the s- and t-channel cross sections simultaneously. A sensitivity study of the measurement for a future dataset with an integrated luminosity of 1 fb^{-1} is conducted.

The thesis is organized as follows. In Chapter 1 the Standard Model of elementary particles and the underlying theory of top-quark production is briefly discussed. The CDF II experiment at the Fermilab Tevatron and its simulation is described in Chapter 2. In Chapter 3 we give a short description of the MadEvent MC samples and we illustrate the matching of the t-channel signal samples. The validation of the samples and the description of the used software (ZTOP) is presented in Chapter 4. Chapter 5 covers the estimate of the systematic uncertainty on the signal modeling. Finally, a sensitivity study for the single-top cross section measurement is done in Chapter 6. The thesis concludes in Chapter 7 with suggestions for improvements of the single-top MC production and an outlook on future cross section measurements.

Contents

1 Top Quark Production within the Standard Model **1**
1.1 The Standard Model 1
1.2 $t\bar{t}$ Production 4
1.3 Single-Top Quark Production 5

2 The CDF II Experiment **9**
2.1 The CDF II Detector 11
2.2 The CDF II Simulation 14

3 Matching of the MadEvent Monte Carlo Samples **17**
3.1 Cross Section based Matching 18
3.2 Slope based Matching 18
3.3 Fraction based Matching 19

4 Validation of the MadEvent Monte Carlo Samples **23**
4.1 ZTOP Software 23
4.2 Validation 24
4.2.1 s-channel Sample 24
4.2.2 t-channel Sample 27

5 Estimate of Systematic Uncertainty on the MC Model **33**
5.1 s-channel Estimate 35
5.2 t-channel Estimate 37

6 Sensitivity of Single-Top Cross Section Measurement **41**
6.1 Single-Top Preselection 42
6.2 Neural Networks 44
6.3 Templates for Signal and Background 49
6.4 Simultaneous Likelihood-Fit of the Single-Top Cross Sections 56

7 Conclusions and Outlook **63**

List of Figures

1.1 Feynman diagram of electron-electron scattering 3
1.2 The CTEQ5M1 parton distribution function at $\mu^2 = (175\ \text{GeV})^2$ . . . 3
1.3 Some leading-order Feynman diagrams of top quark pair production . 4
1.4 Leading-order Feynman diagrams of single-top production modes . . 5
1.5 Top quark polarization visible in angular distribution of single-top MC signal and background 6
1.6 Some NLO Feynman diagrams of s-channel single-top production . . 7
1.7 Some NLO Feynman diagrams of t-channel single-top production . . 7

2.1 Aerial shot of the Tevatron main ring. 9
2.2 Delivered and recorded integrated luminosity since the start of run II 10
2.3 The CDF II detector shortly before the start of Run II 11
2.4 Elevation view of one half of the CDF II detector 12

3.1 Matching procedure of the $m_t = 178\ \text{GeV}/c^2$ sample 18
3.2 Matching with slope minimization of the $m_t = 175\ \text{GeV}/c^2$ sample . . 19
3.3 Intermediate step of the matching of the $m_t = 175\ \text{GeV}/c^2$ sample . . 20
3.4 2nd-b quark p_T of unmatched MadEvent 2→2 LO and 2→3 NLO samples 20
3.5 Final matching of the $m_t = 175\ \text{GeV}/c^2$ sample 21

4.1 s-channel top quark transverse momentum p_T and lepton charge times top quark pseudorapidity $Q_l \cdot \eta$ 24
4.2 s-channel: p_T of 1st-b quark versus p_T of 2nd-b quark and ratio of jet energy of clustered particles coming from B hadrons 25
4.3 s-channel leading jet (j1) p_T and $Q_l \cdot \eta$ 26
4.4 s-channel 2nd-leading jet (j2) p_T and $Q_l \cdot \eta$ 26
4.5 t-channel top quark transverse momentum p_T and lepton charge times top quark pseudorapidity $Q_l \cdot \eta$ 27
4.6 p_T and $Q_l \cdot \eta$ of the t-channel leading b quark jet (b1). 28
4.7 p_T and $Q_l \cdot \eta$ of the t-channel leading light quark jet (q1). 28
4.8 p_T and $Q_l \cdot \eta$ of the t-channel 2nd-leading b quark jet (b2) 29
4.9 p_T and $Q_l \cdot \eta$ of the t-channel 2nd-leading light quark jet (q2) 29
4.10 t-channel: p_T of 1st-b quark versus p_T of 2nd-b quark and ratio of jet energy of clustered particles coming from B hadrons 30
4.11 p_T and $Q_l \cdot \eta$ of the clustered 2nd-leading light jet (q2) in the t-channel 31
4.12 p_T and $Q_l \cdot \eta$ of the matched t-channel 2nd-b jet (2nd b=b1+b2) . . . 31

5.1 Intermediate steps by building the ratio-functions 34
5.2 Ratio-functions of the s-channel 35
5.3 s-channel correlation-matrices of the ratio-functions 36
5.4 Scales of the s-channel events passing the 2+3-jet-bin preselection . . 36
5.5 Ratio-functions of the t-channel t, b1 and q1 37
5.6 Ratio-functions of the t-channel b2 and q2 38
5.7 t-channel correlation-matrices of the ratio-functions: t, tb1 and tq1 . 38
5.8 t-channel correlation-matrices of the ratio-functions: tb1q2, tq1b2 and tq1q2 39
5.9 Scales of events passing the 2+3-jet-bin preselection 39

6.1 The geometry of a 3 layer neural network and the NeuroBayes® sigmoid function 45
6.2 Some of the input variables for the neural net 47
6.3 Some of the input variables for the neural net 48
6.4 2-jet-bin NN Output of background 49
6.5 3-jet-bin NN Output of background 50
6.6 2-jet-bin 2D NN Output and 1D template of t-channel 51
6.7 2-jet-bin 2D NN Output and 1D template of s-channel 51
6.8 2-jet-bin 2D NN Output and 1D template of the background samples 52
6.9 3-jet-bin 2D NN Output and 1D template of t-channel 53
6.10 3-jet-bin 2D NN Output and 1D template of s-channel 53
6.11 3-jet-bin 2D NN Output and 1D template of the background samples 54
6.12 Stacked 2-jet-bin 2D NN Output and stacked 1D templates of all samples 55
6.13 Stacked 3-jet-bin 2D NN Output and stacked 1D templates of all samples 55
6.14 Distribution of generated pseudo events for data 58
6.15 Distribution of generated pseudo events for t-channel signal 58
6.16 Distribution of generated pseudo events for s-channel signal 58
6.17 Distribution of generated pseudo events for $t\bar{t}$ background 59
6.18 Distribution of generated pseudo events for charm background 59
6.19 Distribution of generated pseudo events for non-charm background . . 59
6.20 Pseudo experiment distribution of s-channel and t-channel cross section measurement 60
6.21 Pseudo experiment 2D-distribution of t- vs. s-channel cross section measurement with additional 1σ contour of the fit estimate of a selected individual pseudo experiment 61

List of Tables

1.1 The four fundamental forces in nature and their most important characteristics. 1
1.2 Properties of the fermions (spin-$\frac{1}{2}$ particles) 2
1.3 Properties of the gauge bosons (spin-1 particles) 2

4.1 Summary of all relevant s-channel cross sections and resultant fractions 27
4.2 Summary of all relevant t-channel cross sections and resultant fractions 32

5.1 Summary of the s-channel estimate 36
5.2 Summary of the t-channel estimate 40

6.1 Monte Carlo signal and background samples used in this study 42
6.2 Number of events of the signal and background MC samples passing the preselection cuts 43
6.3 Number of expected events of the signal and background MC samples passing the preselection cuts 44

Chapter 1

Top Quark Production within the Standard Model

1.1 The Standard Model

At present there are four fundamental forces considered by the vast majority of physicists to be the generators of any known interaction in nature: the strong force, the electromagnetic force, the weak force and gravitation (Table 1.1).

force	couples with	effect	rel. strength	range
strong	color charge	binds quarks and gluons	10^0	10^{-15} m
electro-magnetic	electric charge	interaction between el. charged particles	10^{-2}	infinite
weak	weak charge	radioactive decay	10^{-5}	10^{-18} m
gravitation	mass	attraction of masses	10^{-38}	infinite

Table 1.1: The four fundamental forces in nature and their most important characteristics [16].

The strong, weak and electromagnetic forces have been successfully combined in a complete theory, the Standard Model of Elementary Particles (SM). Gravitation is not yet included in this concept and is described by the Theory of General Relativity. The SM provides a very elegant theoretical framework using quantum fields to describe the interactions. It has been very successful in predicting a variety of properties of particles and interactions, which have been and are still tested by a great number of experiments. Up to now, no clear evidence has been found that falsifies the SM, even though we know that it has some weaknesses. Recent results show for example that a very large amount of matter and energy (called Dark Matter and Dark Energy) in the universe is not explained [17, 18].
The Standard Model introduces two kinds of particles, the constituents of matter named fermions, which follow Fermi statistics, and the carriers of the forces named gauge bosons, which have integer spin and follow Bose statistics.

name	category	symbol	el. charge	mass
up	quark	u	$\frac{2}{3}$	$(1.5-4)$
down	quark	d	$-\frac{1}{3}$	$(4-8)$
electron	lepton	e	-1	0.511
e-neutrino	lepton	ν_e	0	$< 3 \cdot 10^{-6}$
charm	quark	c	$\frac{2}{3}$	$(1.15-1.35) \cdot 10^3$
strange	quark	s	$-\frac{1}{3}$	$(80-130)$
muon	lepton	μ	-1	106
μ-neutrino	lepton	ν_μ	0	< 0.190
top	quark	t	$\frac{2}{3}$	$(178.0 \pm 4.3) \cdot 10^3$
bottom	quark	b	$-\frac{1}{3}$	$(4.1-4.4) \cdot 10^3$
tau	lepton	τ	-1	1777
τ-neutrino	lepton	ν_τ	0	< 18.2

Table 1.2: Properties of the fermions (spin-$\frac{1}{2}$ particles) [19]. The electric charge is in units of the electron charge, the mass is in units of MeV/c^2.

The fermions, shown in Table 1.2, consist of the quarks and the leptons and can be ordered in three generations. One generation differs from another only in the mass of the particles, since all other quantum numbers are the same when comparing the corresponding members. Each generation involves two quarks (weak partners), a lepton and its corresponding neutrino. For every constituent of matter we also have to consider the existence of its antiparticle, thus antiquarks and antileptons. The different quark-types are called flavors. Up to now there are six different quark flavors known, up(u), down(d), strange(s), charm(c), bottom(b) and top(t). Quarks carry an additional quantum number in the SM, the color charge, which comes in three different types: red, green or blue. Since the color cannot be detected in nature, the quarks must be confined into colorless particles called hadrons, which are classified into baryons (three quark states) and mesons (quark-antiquark states). The gauge bosons and some of their properties are listed in Table 1.3.

name	force	symbol	el. charge	mass
gluon	strong	g	0	0
photon	electromagnetic	γ	0	0
W boson	weak	$W^\pm$	± 1	80.425 ± 0.038
Z boson	weak	Z^0	0	91.188 ± 0.002

Table 1.3: Properties of the gauge bosons (spin-1 particles) [19]. The electric charge is in units of the electron charge, the mass is in units of GeV/c^2.

The interactions between charged particles are described by Feynman diagrams. Forces between the interacting particles (quarks and leptons) are mediated by gauge bosons that are emitted and reabsorbed. As an example the diagram for electron-

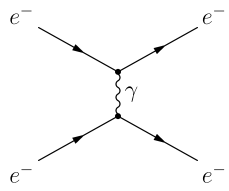

Figure 1.1: Feynman diagrams of electron-electron scattering. At the left hand side are the two incoming initial state electrons. They interact via a virtual photon (γ) and the scattered final state electrons phase out to the right. The coupling of the electrons to the photon depends on the vertices, shown in the diagram by the dots.

electron scattering via the exchange of a virtual photon is shown in figure 1.1. The Feynman diagram gives a visualization of the physical process in the momentum space at parton level. Only elementary particles (quarks, leptons and bosons), called partons in this context, are allowed to interact with each other. The Feynman rules provide a prescription of how to translate the diagram into a formula to calculate the transition amplitude $\mathcal{M}$. From this the cross section of the process can be derived by integrating over all initial and final states, the phase space.
When comparing to experiments, one has to take care whether the incoming particles are leptons or hadrons composed of quarks and gluons. The calculation of Feynman diagrams is based on partons as initial states. Protons and antiprotons colliding at the Fermilab Tevatron are composite particles. The proton is made of three valence quarks (uud), held together via the exchange of virtual gluons. These gluons can split into a quark-antiquark pair, the seaquarks. This leads to the situation, that the momentum of the proton p_p is shared by all three valence quarks, sea-quarks and gluons. The fraction of the momentum $x_i = \frac{p_i}{p_p}$, carried by each quark and gluon, is described by the parton distribution function (PDF) $f_{i,p}(x_i, \mu^2)$ [20]. It depends on the scale μ, which for top quark production is usually set to the order of the top quark mass, $\mu = m_t$. Figure 1.2 shows the CTEQ5M1 parton distribution function for the scale $\mu^2 = (175\text{ GeV})^2$. These PDFs have to be folded with the partonic cross sections to calculate the measurable cross section in $p\bar{p}$ collisions.

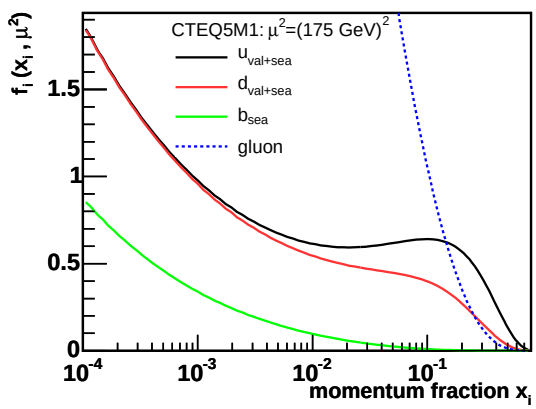

Figure 1.2: The CTEQ5M1 parton distribution function at $\mu^2 = (175\text{ GeV})^2$ [20].

When dealing with electroweak processes containing quarks, one has to be aware of the fact that the mass eigenstates are not equivalent to the flavor eigenstates. This was experimentally found and is implemented in the theory by flavor-mixing. All three quark generations form the Cabbibo-Kobayashi-Maskawa matrix (CKM-matrix) [21, 22]. It is expressed by a 3×3 unitary matrix V:

$$\begin{pmatrix} d' \\ s' \\ b' \end{pmatrix} = \begin{pmatrix} V_{ud} & V_{us} & V_{ub} \\ V_{cd} & V_{cs} & V_{cb} \\ V_{td} & V_{ts} & V_{tb} \end{pmatrix} \begin{pmatrix} d \\ s \\ b \end{pmatrix} \tag{1.1}$$

The single elements of this matrix have to be determined experimentally. $V_{q_1 q_2}$ is proportional to the coupling of two quarks q_1, q_2 to a W boson. The current values (90% confidence level) [19] for the different elements $V_{q_1 q_2}$ are given in (1.2).

$$\begin{pmatrix} 0.9739 \text{ to } 0.9751 & 0.221 \text{ to } 0.227 & 0.0029 \text{ to } 0.0045 \\ 0.221 \text{ to } 0.227 & 0.9730 \text{ to } 0.9744 & 0.039 \text{ to } 0.044 \\ 0.0048 \text{ to } 0.014 & 0.037 \text{ to } 0.043 & 0.9990 \text{ to } 0.9992 \end{pmatrix} \tag{1.2}$$

1.2 $t\bar{t}$ Production

In proton-antiproton ($p\bar{p}$) collisions at the Fermilab Tevatron, the dominant top quark production mode is $t\bar{t}$ pair production via the strong interaction. Even though $t\bar{t}$ pairs can be produced via the electroweak interaction through an exchange of a Z^0 boson or photon, this contribution is negligible compared to the strong QCD cross section. Figure 1.3 shows some leading order Feynman diagrams for $t\bar{t}$ production. At a symmetric $p\bar{p}$ collider, the square of the center-of-mass energy of the interacting partons is defined by $\hat{s} = (x_1\mathcal{P}_p + x_2\mathcal{P}_{\bar{p}})^2 = 4x_1x_2\mathcal{P}_p^2 = x_1x_2s$, where s is the square of the center-of-mass energy of the colliding hadrons and $\mathcal{P}$ the 4-momentum of the participating hadrons. At energies above the kinematic threshold of $t\bar{t}$ production $\hat{s}_{min} = (\mathcal{P}_t + \mathcal{P}_{\bar{t}})^2 = 4m_t^2$ at the Tevatron ($\sqrt{s} = 1.96$ TeV), the momentum fractions of the partons are given by $x_1x_2 \geq \frac{\hat{s}_{min}}{s} = \frac{4m_t^2}{(1.96 \text{ TeV})^2} \approx 0.032 \approx (0.18)^2$. In this region of x_i and above, the incoming partons are mostly valence quarks, as visible in the PDFs (Figure 1.2). Therefore, $80 - 90\%$ of the cross section is due to quark-antiquark annihilation (Figure 1.3 (a)).

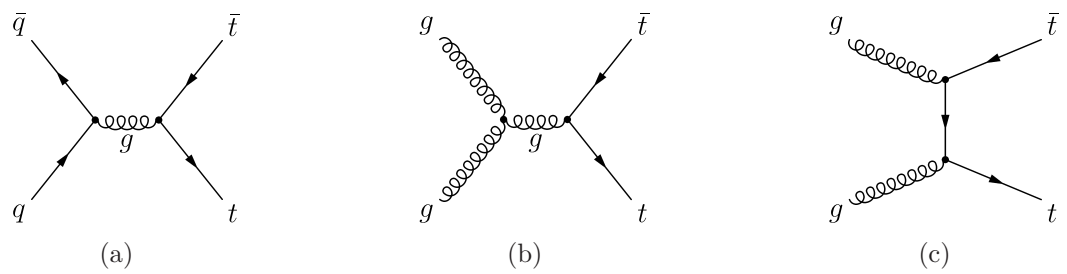

Figure 1.3: Some leading-order Feynman diagrams of top quark pair production: quark-antiquark annihilation (a) and gluon fusion (b), (c).

The corresponding cross section calculation, as discussed earlier, is based on the factorization theorem, i.e. the PDFs $f_{i,a}(x_i, \mu^2)$ of the incoming hadrons $ab = p\bar{p}$ have to be folded with the cross section $\hat{\sigma}_{ij}$ of the initial partons $ij = q\bar{q}$:

$$\sigma(ab \to t\bar{t}) = \sum_{i,j} \int \mathrm{d}x_i \mathrm{d}x_j f_{i,a}(x_i, \mu^2) f_{j,b}(x_j, \mu^2) \cdot \hat{\sigma}_{ij}(ij \to t\bar{t}) \tag{1.3}$$

The parton-parton cross section $\hat{\sigma}_{ij}$ can be calculated as a perturbation series in the strong QCD running coupling constant $\alpha_s(\mu^2)$. The differential cross section for leading-order quark-antiquark annihilation, which contributes with α_s^2 to the perturbation series, is given by:

$$\frac{\mathrm{d}\hat{\sigma}}{\mathrm{d}\hat{t}}(q\bar{q} \to t\bar{t}) = \frac{4\pi\alpha_s^2}{9\hat{s}^4} \cdot \left[(m_t^2 - \hat{t})^2 + (m_t^2 - \hat{u})^2 + 2m_t^2\hat{s}\right], \tag{1.4}$$

where $\hat{s} = (\mathcal{P}_q + \mathcal{P}_{\bar{q}})^2$, $\hat{t} = (\mathcal{P}_q - \mathcal{P}_t)^2$ and $\hat{u} = (\mathcal{P}_q + \mathcal{P}_{\bar{t}})^2$ are the invariant Mandelstam variables of the process with $\mathcal{P}_i$ being the corresponding momentum 4-vector of the quark i.
The current next-to-leading-order calculations of the $t\bar{t}$ production cross section at the Tevatron Run II center-of-mass energy of $\sqrt{s} = 1.96$ TeV, with a top quark mass of $m_t = 175$ GeV/c^2, give 6.7 ± 0.9 pb [23, 24].

1.3 Single-Top Quark Production

For the electroweak production of single-top quarks, two modes are dominating at the Fermilab Tevatron: the t-channel process (Figure 1.4 (a)) with a total NLO cross section of $1.98^{+0.28}_{-0.22}$ pb and the s-channel process (Figure 1.4 (b)), also called W^* production (0.88 ± 0.11 pb at NLO) [25, 15]. In $p\bar{p}$ collisions the third electroweak production mode, the associated production (Figure 1.4 (c)), known as Wt production, has by comparison a small cross section of $0.094^{+0.015}_{-0.012}$ pb (no full NLO calculation) [26]. All indicated cross sections are calculated with a top mass of 175 GeV/c^2.

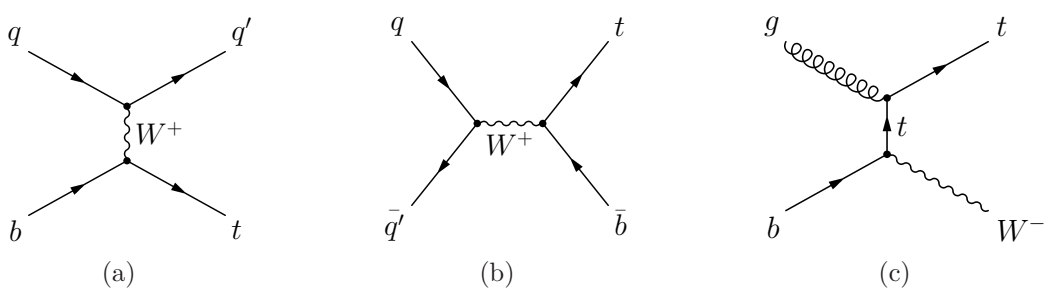

Figure 1.4: Leading-order Feynman diagrams of single-top production modes: t-channel (a), s-channel (b) and associated production (c).

All three production modes are distinguished by the virtuality $Q^2 = -q^2$, where q is the 4-momentum of the participating W boson. The two dominating processes are labeled by the Mandelstam variable involved in the transition matrix element. In t-channel production a spacelike (virtual) W boson ($q^2 = \hat{t} < 0$) strikes a b quark inside the proton or antiproton, whereas in s-channel production a timelike W boson ($q^2 = \hat{s} \geq (m_t + m_b)^2$) is produced by the fusion of two quarks. In the associated production an on-shell (or close to on-shell) W boson ($q^2 = m_W^2$) is produced in conjunction with the top quark. There are also other electroweak production modes than those involving the Wtb vertex. But the channels involving a Wtd or Wts vertex are strongly suppressed since the involved CKM matrix elements as seen in (1.1) and (1.2) are tiny. The contribution of such processes to the total single-top cross section is about 1% and thus negligible at the Tevatron. The same circumstance is valid for the top quark decay. Nearly 100% decay into a b quark and a W boson. Decays into d or s quarks are strongly CKM suppressed.

In s- and t-channel production the top quarks are produced 100% polarized along the direction of the down-type quark (q' in Figure 1.4 (a), (b) and 1.7 (a)) in the top quark rest frame [27, 28, 29]. This is due to the fact that the W boson couples only to left-handed fermions. This polarization can be measured since top quarks decay before the typical time scale for hadronization is reached. Hadronization describes the transition from partons to hadrons, and in this stage information such as polarization is typically lost. Consequently, the decay products of the top quark, especially the W boson, carry the polarization information. A good variable to investigate experimentally is the angle $\Theta_{l,q}$ between the lepton, coming from the W boson decay, and the light quark jet axis in the top quark rest frame. As shown for reconstructed MC events in Figure 1.5, the top quark polarization can be used to discriminate between t-channel single-top signal and background.

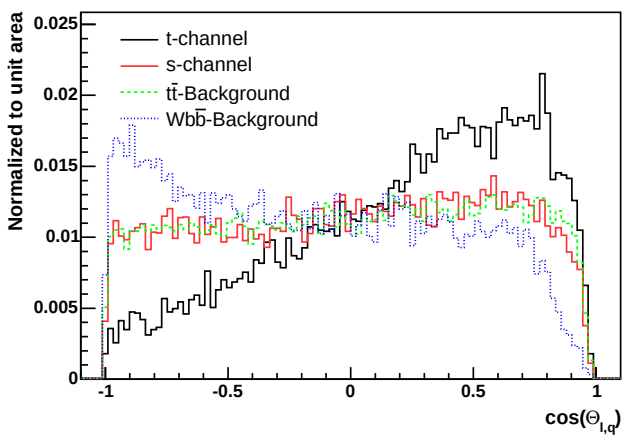

Figure 1.5: Top quark polarization visible in angular distribution of single-top MC signal and background: $\cos(\Theta_{l,q})$ between lepton and light quark jet axis in the top quark rest frame is a discriminating variable especially for the t-channel.

The NLO contributions to the s-channel, shown in Figure 1.6, will mostly lead to additional soft light quarks, since the probability of the gluon to split into a heavy quark antiquark pair is quite low.

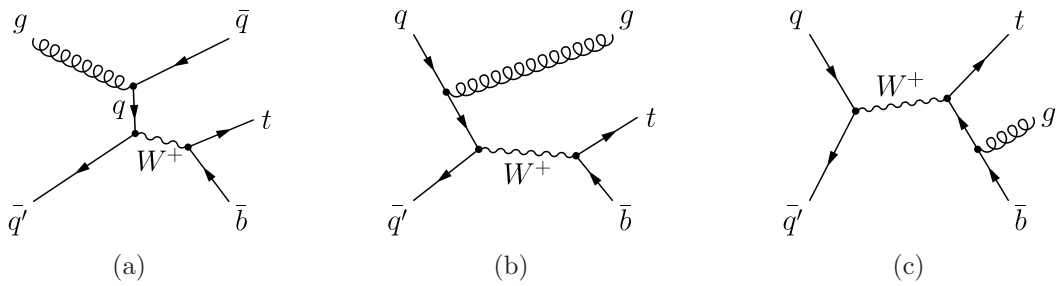

Figure 1.6: Some NLO Feynman diagrams of s-channel single-top production: initial state gluon splitting (a), initial state gluon radiation (b) and final state gluon radiation (c).

The most important NLO correction to the t-channel leading-order process shown in Figure 1.4 (a) is the 2→3 process, which is known as W-gluon fusion, where an initial gluon splits into a $b\bar{b}$ pair (Figure 1.7 (a)).

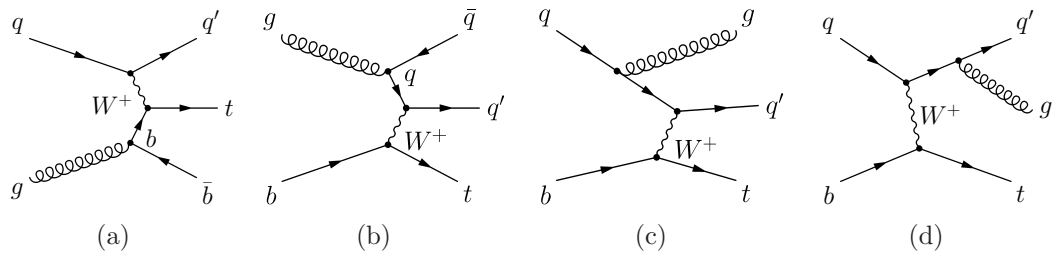

Figure 1.7: Some NLO Feynman diagrams of t-channel single-top production: W-gluon fusion (a), initial state gluon splitting (b), initial state gluon radiation (c) and final state gluon radiation (d).

If the b quark is considered massless in the computation of the W-gluon fusion matrix element, the gluon splits into a real $b\bar{b}$ pair with the final state $\bar{b}$ quark (in the following called 2nd-b quark in order to distinguish from the b quark coming from the decay of the top quark) being collinear with the incoming gluon. Given that the internal b quark is on-shell, its propagator is infinite and the Feynman diagram becomes singular. As in reality the b quark is not massless, its mass m_b regulates the collinear singularity, which is described by terms of $ln[(Q^2+m_t^2)/m_b^2]$, where Q^2 is the virtuality of the W boson. The W-gluon fusion cross section contains these logarithmic terms of order $ln^n[(Q^2+m_t^2)/m_b^2]/n!$ at every order n of the perturbative expansion in the strong coupling due to the collinear emission of gluons from the internal b quark propagator. This leads to the fact that, since the logarithms are large, the perturbation series does not converge quickly.

However, by introducing a b quark distribution function, one can sum up all collinear logarithms and bypass the convergence difficulty. Due to this method the cross

section of the process in Figure 1.4 (a) is of order $ln[(Q^2 + m_t^2)/m_b^2]$, the diagram in Figure 1.7 (a) also contains these terms, even though they are already summed into the b quark distribution function. So, to avoid double counting, one needs to remove these terms. This subtraction method, carried out in reference [30], achieves the same results within the errors as the phase space slicing method [25], upon which the ZTOP software is based. This analytic form of the NLO cross section calculation is fully differential, therefore experimental cuts can be implemented.

Chapter 2

The CDF II Experiment

The CDF II experiment is located at the Tevatron collider at the Fermi National Laboratories (Fermilab) in the western vicinity of Chicago, Illinois (USA). The Tevatron is the accelerator with the highest center-of-mass energy currently in operation, here protons and antiprotons circulate in opposite directions in a ring with a diameter of 2 km. The first collisions at a center-of-mass energy of 1.8 TeV were initiated in 1985. The data collected until 1996 in the so called Run I phase amount to 130 pb^{-1} and allowed, among other interesting results, the first experimental evidence of the top quark, followed by the precise determination of its mass. Starting in 1996, the accelerator complex was upgraded to increase the instantaneous luminosity and the center-of-mass energy. CDF and DØ, the second Tevatron experiment, were upgraded as well. The Run II phase started at the end of 2001 and is scheduled until 2009.
In Run II, protons and antiprotons are brought to collisions at a center-of-mass energy of 1.96 TeV. To reach this, a system of different accelerators is needed. The first step in the accelerator chain is the Cockcroft-Walton pre-accelerator. Hydrogen

Figure 2.1: Aerial shot of the Tevatron main ring. The CDF site in this view is located at the eight o'clock position direct at the outside of the ring, the DØ site is at the twelve o'clock position. The Fermilab main building is visible in the foreground.

gas is ionized to create negative ions that are accelerated by a positive voltage to an energy of 750 keV. The negative ions then enter a linear accelerator, called LINAC, about 130 m long which accelerates the ions by means of an oscillating electric field to 400 MeV. The ions then pass a carbon foil, where the electrons are stripped off. The next step is the booster, a circular accelerator that uses magnets to bend the beam of protons in a circular path. After some 20.000 revolutions, the protons leave the booster with an energy of 8 GeV. Protons are then transferred to the Main Injector where they are accelerated from 8 GeV to 150 GeV.
To produce the antiprotons, the Main Injector sends 120 GeV protons to the Antiproton Source, where the protons collide with a nickel target. The collisions produce a wide range of secondary particles including many antiprotons. The antiprotons are collected, focused and then stored in the Accumulator ring. When a sufficient number of antiprotons has been produced, they are sent to the Main Injector for further acceleration up to 150 GeV.
The last step in the long chain of accelerators to reach the 1.96 TeV energy is the Tevatron accelerator and storage ring, a collider with a circumference of about six kilometers. Protons and antiprotons are circulating in opposite directions at 0.98 TeV and are brought to collision at two interaction points: DØ and BØ (where CDF is located).
The energies of the protons and antiprotons determine the cross section σ of the physical processes one wants to observe. The number n of produced events in a given period is given by $n = \sigma \int \mathcal{L}\ \mathrm{dt}$. The quantity $\mathcal{L}$ is called instantaneous luminosity, the quantity $\int \mathcal{L}\ \mathrm{dt}$ is the integrated luminosity over time.
In the beginning of Run II in June 2001, the instantaneous luminosity did not meet the design goals, partially because the new main injector was not well understood and under control. As knowledge about the accelerators grew, also the instantaneous luminosity increased. The amount of data delivered by the Tevatron and written to tape is presented as a function of time in Figure 2.2.

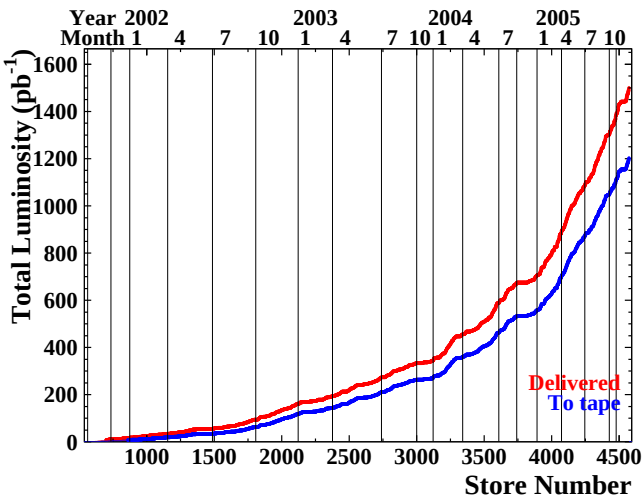

Figure 2.2: Delivered (upper curve) and recorded to tape (lower curve) integrated luminosity since the start of Run II.

It is planned to continue the Tevatron operation until the end of the fiscal year 2009. The baseline goal is to achieve an integrated luminosity of 4.4 fb^{-1}, the design luminosity goal is 8.4 fb^{-1}. As it looks now, the design luminosity will be reached, the design luminosity for the end of fiscal year 2005 was 1.2 fb^{-1}, a goal that was reached.

2.1 The CDF II Detector

The CDF II experiment (see Figure 2.3) is a general purpose solenoidal detector measuring the collisions of protons and antiprotons at the Tevatron. It covers most of the 4π space angle around the beam spot and feature azimuthal and forward-backward symmetry. It can measure the tracks made by charged particles in the core of the detector, the energy deposit in calorimeters and identify muons. Magnetic fields help identifying charged particles. Some components of CDF and the data acquisition system have been upgraded for Run II to deal with the increased instantaneous luminosities. In addition to this, the coverage and capabilities of the existing subdetectors have been extended. A more detailed description of the CDF II detector can be found in its technical design report [31].
The detector was built and is maintained by a collaboration of more than 50 institutions in eleven countries. The Institut für Experimentelle Kernphysik in Karlsruhe is the only German institute in the CDF collaboration and member since 1996.

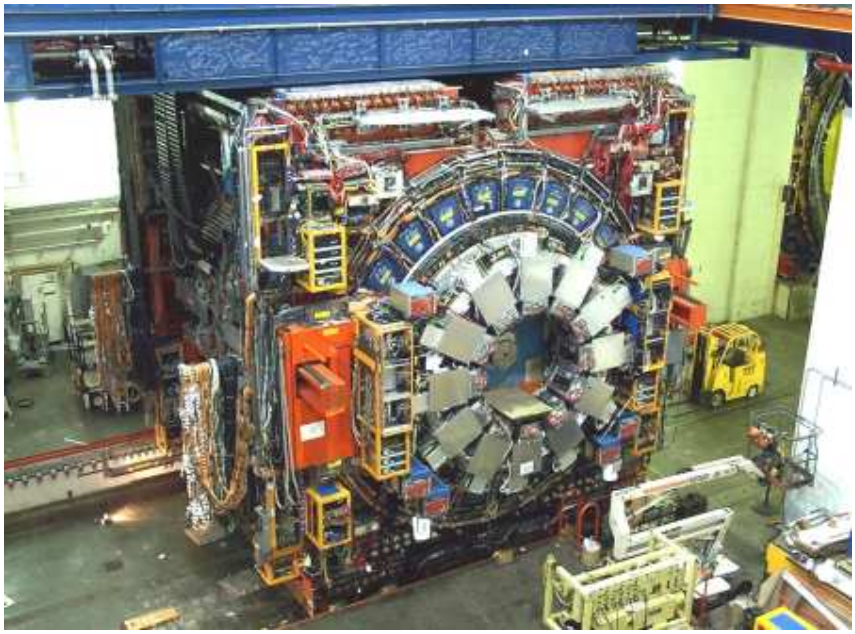

Figure 2.3: The CDF II detector shortly before the start of Run II.

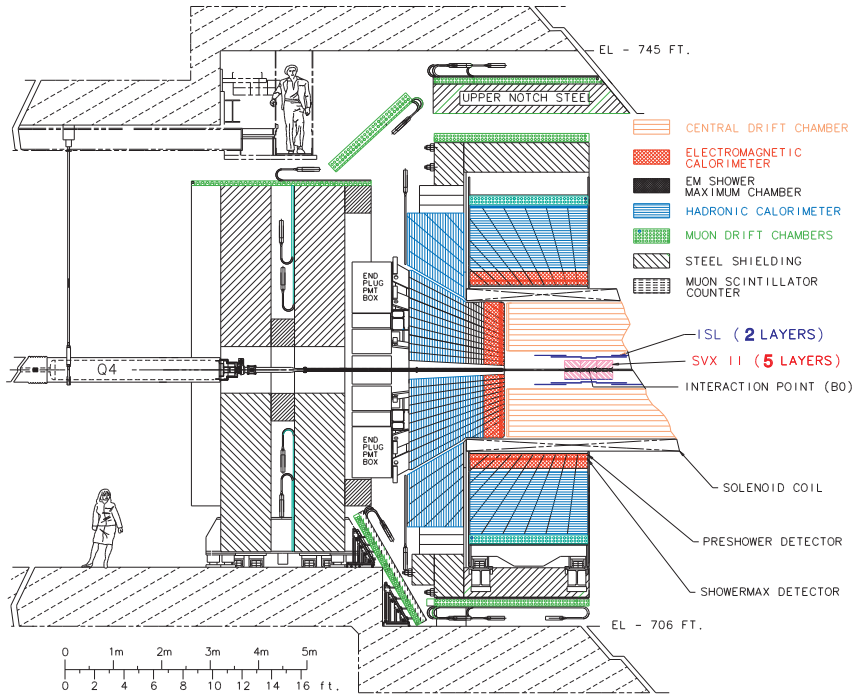

Figure 2.4: Elevation view of one half of the CDF II detector.

Figure 2.4 shows an elevation view of one half of the CDF II detector. In the following, angles and directions are often referred to the CDF coordinate system. The polar angle θ is measured with respect to the proton beam axis (z-axis), pointing in east direction. The azimuthal angle φ is measured from the plane of the Tevatron. Transverse and longitudinal are meant with respect to the proton beam, i.e. parallel and perpendicular to the proton beam respectively. An often-used quantity is the pseudorapidity defined by $\eta = -\ln\left(\tan\frac{\theta}{2}\right)$.

The Tracking System in Run II consists of 4 parts: Layer 00, the SVX II (Silicon Vertex Detector), the ISL (Intermediate Silicon Layers) and the COT (Central Outer Tracker), which is an open drift chamber. Glued to the beam pipe, Layer 00 is closest to the beam, with its modules placed at radii $r = 1.35$ cm and $r = 1.62$ cm of the beam pipe. It is a single-sided radiation hard silicon microstrip detector and provides a coverage of $|\eta| < 4.0$. Layer 00 was added later to the design of the vertex detector to enhance its resolution and longevity.
Layer 00 is enclosed by the the SVX II. The SVX II detector design is driven by high luminosity, the Tevatron short bunch spacing of 396 ns and by the physics requirement of B hadron decay vertex identification within collimated high-P_T jets. SVX II is comprised of three cylindrical barrels which cover $\approx 2.5\sigma$ of the interaction region providing track information to pseudorapidity $|\eta| < 2$. Five layers of double-sided silicon sensors at radii from 2.4 to 10.7 cm supply $r - \varphi$ as well as 3 $r - z$ and 2 small angle stereo measurements. The results provide good pattern recognition and 3-d vertex reconstruction with an impact parameter resolution $\sigma_\varphi < 30\mu$m

and $\sigma_{z0} < 70\mu m$ for central high momentum tracks. The impact parameter is the distance of closest approach of the track helix to the beam axis measured in the plane perpendicular to the beam. The SVX II provides coverage up to $|\eta| \approx 2$. In the region $|\eta| < 1$ the combination of the SVX II and the COT can provide full 3D tracking, but the reconstruction will need to be anchored on COT tracks. For $|\eta| > 1$, SVX II can only allow for 2D tracking. To increase the the tracking volume, the three layers of the silicon detector ISL are placed between the SVX II and the COT.
The outer part of the tracking system is the Central Outer Tracker, a 3.1 m long cylindrical open drift chamber, to provide tracking at large radii in the region $|\eta| < 1.0$. The COT covers the radial range from 40 to 137 cm and provides 96 measurement layers organized into alternating axial and ± 2 stereo superlayers. The hit position resolution is approximately $14\mu m$ and the momentum resolution $\sigma(p_T)/p_T^2 = 0.0015(GeV/c)^{-1}$. Due to the high luminosity and the short bunch spacing, the COT is designed to operate with a maximum drift time of 100 nsec by reducing the maximum drift distance and by using a gas mixture with a fast drift velocity.

Between the COT and the solenoid, a Time-of-Flight system (TOF) is installed mainly for particle identification. It consists of scintillator panels which provide both timing and amplitude information. The timing resolution is 100 ps. The detector covers the central region out to $|\eta| < 1.1$ and is capable of distinguishing kaons from pions by their flight time difference with at least 2σ separation up to kaon momenta of 1.6 GeV/c.

A superconducting solenoid, 1.5 m in radius and 4.8 m in length, is surrounding the tracking volume. It generates a 1.4 T magnetic field parallel to the beam axis for measuring the transverse momentum of charged particles.

The solenoid and tracking volume is surrounded by the calorimeters, designed to measure the energy of particles and jets by fully absorbing all particles except muons and neutrinos. There are, altogether, five calorimeter systems: the central electromagnetic calorimeter (CEM), the central hadron calorimeter (CHA), the end-wall hadron calorimeter (WHA), the end-plug electromagnetic (PEM) and hadron calorimeter (PHA), covering 2π in azimuth and pseudorapidity $|\eta| < 3.6$. Each calorimeter module is divided into projective towers, pointing to the nominal interaction point. The calorimeters are sampling calorimeters. The active medium is a scintillator, the absorber is lead in the electromagnetic calorimeter and iron in the hadronic calorimeter.

Four systems of scintillators and drift tubes are used to detect muons. The central calorimeters act as a hadron absorber for the Central Muon Detection System (CMU). The CMU consists of four layers of drift chambers located outside the central hadronic calorimeter. Its range is $|\eta| < 0.6$ and can be reached by muons with transverse momenta greater than 1.4 GeV/c. Four additional layers of drift cham-

bers are located behind a 0.6 m thick absorber layer of steel. This system is called Central Muon Upgrade (CMP). The CMP covers the same η range. In addition, the pseudorapidity range of $0.6 < |\eta| < 1.0$ is covered by the Central Muon Extension (CMX). These systems have been used already in Run I, however, new chambers have been added to the CMP and CMX in order to close gaps in the azimuthal coverage. The Run I forward muon system has been replaced by the Intermediate Muon System (IMU) covering a range of $1.0 < |\eta| < 1.5$.

The trigger system plays an important role to efficiently extract the most interesting physics events from the large number of minimum bias events, because the collision rate is equal to the mean crossing rate of 1.7 MHz while the tape writing speed is about 75 Hz at present. The CDF trigger is a three level system with each level providing a sufficient rate reduction for the processing of the next level.
The first two triggers are hardware triggers, the last one is a software trigger running on a Linux PC farm. Level-1 uses custom designed hardware to find physics object based on a subset of the detector. The hardware consists of three parallel synchronous processing streams: one to identify calorimeter based objects, another one to identify muons while the third one does tracking in the COT using the eXtremly Fast Tracker (XFT). The decision is done by simple counting these objects (e.g. one electron with 12 GeV). If an event is accepted by the Level-1 trigger, the data are moved to one of the four on-board Level-2 buffers, to average out the rate fluctuations. The typical rate of the Level-1 triggers is at present 24 kHz accept rate.
The Level-2 trigger do a limited event reconstruction using a custom-designed hardware. The hardware consists of several asynchronous subsystems, e.g the hardware cluster finder using calorimeter information. In addition, data from the shower maximum detector (CES) can be used to improve the identification of electrons and photons. The most challenging addition for the Level-2 trigger is the Silicon Vertex Tracker. The SVT allows to select tracks with large impact parameter, which opens a complete new window for physics measurements at a hadron collider. The level-2 trigger accepts 300 events per second, which are transferred to the Level-3 processor farm.
At the processor farm the events are reconstructed and filtered, using the algorithms run in the "offline" reconstruction, and are written to permanent storage with approximately 75 Hz at present. To facilitate the handling of the huge data volumes collected with the CDF II detector, events passing the Level-3 trigger are split into eight different streams.

2.2 The CDF II Simulation

The understanding of efficiencies, acceptances and the kinematic properties of signal and background processes requires a deep knowledge of the physics processes and the detector response. Therefore, Monte Carlo generators are used, which randomly generate hard parton interactions of a given process according to the probability

density of phase space. The resulting partons are then processed by a parton showering to simulate gluon radiation and fragmentation. The resulting particles are then handed to the detector simulation. The detector response is modeled on a detailed simulation with the GEANT3 package [32]. To speed up the simulation, the charged particle ionization and drift properties in the COT are parametrized and tuned to data. The development of showers in the various calorimeters is computed by GFLASH, a shower development package. The GFLASH parameters for electromagnetic and hadronic showers are also tuned to data.
The CDF simulation is an integral part of the CDF software framework. In order to further analyze the simulated data, it uses the same algorithms and geometry for event reconstruction and simulation. The CDF geometry contains the detailed description of the silicon detectors (SVX, ISL), the Central Outer Tracker (COT), the muon systems, the Time-of-Flight (TOF) system, the electromagnetic and hadronic calorimeters and further more subdetectors. In addition, several passive material elements are simulated, in particular within the silicon detectors. The format of the simulated data is, with the exception of the HEPG bank containing additional Monte Carlo truth information, identical to the format of real detector data. A detailed description of the CDF II simulation can be found in reference [33].

Chapter 3

Matching of the MadEvent Monte Carlo Samples

The CDF Run I single-top analysis used PYTHIA to generate s- and t-channel MC events. For the t-channel it is known that PYTHIA generates too soft and too far forward distributed 2nd-b quarks. The reason for that is that PYTHIA starts with the LO 2→2 diagram (see Figure 1.4 (a)), i.e. with a b quark PDF and then creates the initial state through backward evolution (DGLAP scheme [34, 35, 36]). Using this method, only the soft region of the transverse momentum of the 2nd-b quark is well modeled, while the hard region is underestimated. To bypass this problem, the CDF Run II single-top analysis chose MadEvent as MC generator, which brings along two advantages:
First, it provides the opportunity to generate two independent t-channel samples, the 2→2 LO process with a b quark PDF to cover the soft p_T range and another 2→3 NLO process (see Figure 1.7 (a)) with an initial state gluon splitting into a $b\bar{b}$ pair for the hard range. Both processes differ in the number of final state partons: the 2→2 matrix element includes the light quark and the decay products of the top quark, namely a lepton, a neutrino and the so-called 1st-b quark in the final state. The 2→3 matrix element includes the same final state partons plus an additional $\bar{b}$ quark, the already mentioned 2nd-b quark.
Second, MadEvent fully incorporates the spin of the top quark in contrast to the PYTHIA generator. As discussed in Chapter 1.3, one interesting feature of electroweak top quark production is that the top quark in its rest frame is almost 100% polarized along the direction of the down-type quark (q' in Figure 1.4 (a), (b) and 1.7 (a)). It is important to include this feature in the Monte Carlo description since it can be used to discriminate single-top-quark events from background.

Because MadEvent is designed to produce events at parton level, one needs a parton showering software to compute all desired final state particles and hadrons. For this purpose PYXTRA was used, a software interface that passes on the MadEvent output to PYTHIA, where a strong-angular-ordered showering is done through emission of QCD radiation.

3.1 Cross Section based Matching

For the upcoming CDF single-top analysis, the s- and t-channel MadEvent MC sample production at the end of 2004 was conducted with a top quark mass set to 178 GeV/c^2, corresponding to the then valid world average. As already addressed, two independent t-channel samples were generated.
A matching of the two MC samples was conducted by the single-top group in such a manner, that an event was accepted, if simultaneously both the p_T of the 2nd-b quark was lower (higher) than a fixed threshold K_T and the event was from the 2→2 LO (2→3 NLO) process. By this procedure, as described in [11], double counting of events from the same phase space is avoided. One obtains a combined t-channel single-top MC sample with a p_T-spectrum of the 2nd-b quark valid in both the soft and the hard region and with a continuous transition between them. The threshold K_T is defined as the intersection of the LO and NLO p_T distributions. To calculate this intersection point, the rates of the LO and NLO distributions were normalized to their respective cross sections obtained from MadEvent [14].
According to the MadEvent calculations, the ratio of the two cross sections was $R = \sigma_{LO}/\sigma_{NLO} = 1.42$. Using this value the intersection point K_T was about 10 GeV (see Figure 3.1 (a)). 144445 events out of the 2→2 sample and 58316 events of the 2→3 sample were merged into the matched MadEvent sample, whose resulting p_T distribution is shown in Figure 3.1 (b).

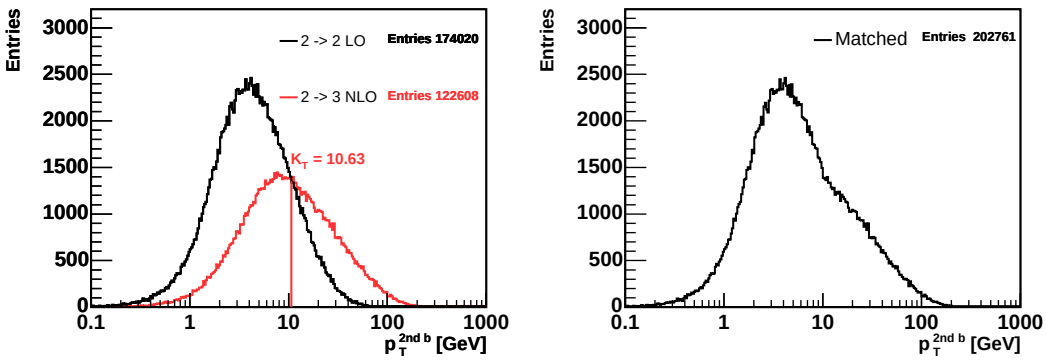

(a) (b)

Figure 3.1: Matching procedure of the $m_t = 178$ GeV/c^2 sample in log_{10} scale: 2nd-b quark p_T of unmatched MadEvent 2→2 LO and 2→3 NLO samples with intersection at about 10 GeV (a), matched sample (b).

3.2 Slope based Matching

During 2005, new top-mass analyses with improved precision were conducted at CDF and DØ. They made clear, that the next, not yet published, world average of the top-mass will move towards a lower value. Thus, the CDF Collaboration decided

to use a top mass of 175 GeV/c^2 for all upcoming analyses. Due to this, new samples had to be produced from the CDF single-top group. In the 178 GeV/c^2 t-channel sample, the rate of the 2nd-b quark jet was found to be too low when comparing to NLO calculations. Since the b quarks contributing to these jets are all from the 2→3 MadEvent sample, which was, compared to the 2→2 sample, scaled down by the cross section ratio $R = \sigma_{LO}/\sigma_{NLO}$ and merged into the matched signal sample, one could improve the fraction between the 2→2 and 2→3 events by introducing a new matching procedure for the new generation. Such a new method is proposed in reference [14].

Instead of using the cross section ratio R, whose physical meaning is ambiguous, the single-top group used the minimum of the differences of the slopes of the two 2nd-b quark p_T distributions at their intersection point K_T in dependence of the ratio R, to find the best mixing ratio, which leads to a smooth transition. The resulting distribution with an intersection at $K_T = 15.2$ GeV and a cross section ratio of $R = \sigma_{LO}/\sigma_{NLO} = 2.09$ is shown in Figure 3.2 (a), the matched sample in (b).

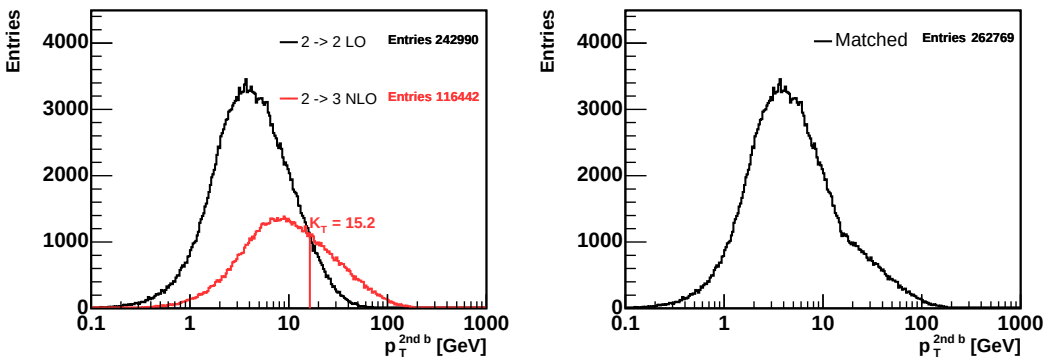

(a) (b)

Figure 3.2: Matching with slope minimization of the $m_t = 175$ GeV/c^2 sample in log_{10} scale: 2nd-b quark p_T of unmatched MadEvent 2→2 LO and 2→3 NLO samples with intersection at 15.2 GeV (a), matched sample (b).

3.3 Fraction based Matching

It is obvious from Figure 3.2, that the new fraction of 2nd-b quarks from the hard region decreases compared to the 178 GeV/c^2 sample, where we found that the rate of the hard 2nd-b quark jets was too low. Therefore a third matching procedure, proposed in reference [15], is conducted. The underlying concept is to vary the ratio $R = \sigma_{LO}/\sigma_{NLO}$, more precisely the fraction of 2→3 events, until the rate of 2nd-b quark jets from the hard region comply to the NLO predictions of the ZTOP software.

In a first pass, we choose a ratio of $R = 1.4$ (about the same as for the 178 GeV/c^2 sample) to be the working point for further estimates. Figure 3.3 shows the associated intersection point at $K_T = 11$ GeV.

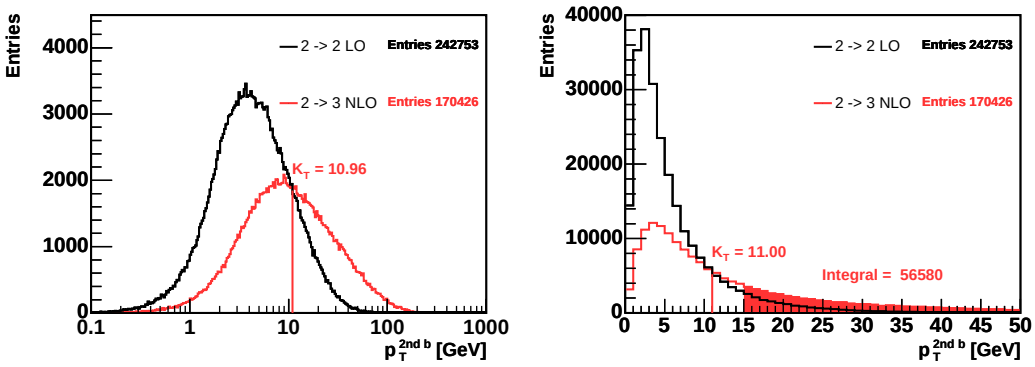

(a) (b)

Figure 3.3: Intermediate step of the matching of the $m_t = 175$ GeV/c^2 sample: 2nd-b quark p_T of unmatched MadEvent 2→2 LO and 2→3 NLO samples (in log_{10} (a) and linear (b) scale) with intersection at 11 GeV.

In the second pass, a new R ratio is estimated, which should meet the following prediction of the NLO calculation: within the detector cuts, a 2nd-b quark jet appears in 21.1% of all events. The detector cuts, motivated by the single-top analysis, are $p_T > 15$ GeV and $|\eta| < 2.8$. To fulfill this NLO prediction, the MadEvent $R = 1.4$ sample should have about 59800 visible 2nd-b quarks out of the total of 283410 events. As highlighted in Figure 3.3 (b), 56580 events include a 2nd-b quark with $p_T > 15$ GeV, whereof about 98.5% pass the $|\eta| < 2.8$ cut.

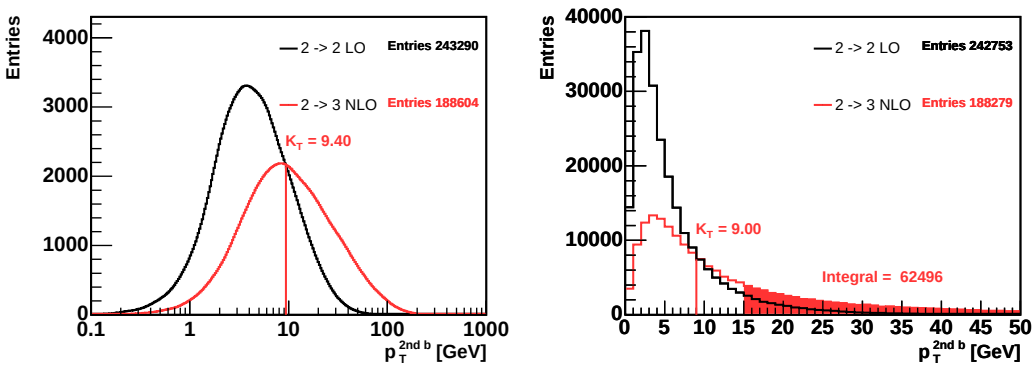

(a) (b)

Figure 3.4: 2nd-b quark p_T of unmatched MadEvent 2→2 LO and 2→3 NLO samples: intersection at 9 GeV in smoothed log_{10} distribution (a), in linear scale (b).

By increasing the fraction of 2→3 events from 170426 to 188279 and thereby decreasing the ratio from $R = 1.4$ to $R = 1.29$, appropriate matching parameters are found. The value of $K_T = 9$ GeV, the nearest integer at the intersection of the smoothed distributions of the sub-samples (Figure 3.4 (a)), results in 62496 2nd-b quarks with $p_T > 15$ (highlighted in Figure 3.4 (b)). 61521 of them pass the $|\eta| < 2.8$ cut, which exactly matches the NLO predictions of 21.1% of the total of 291738 events. The resulting sub-samples and the matched t-channel sample are shown in Figure 3.5.

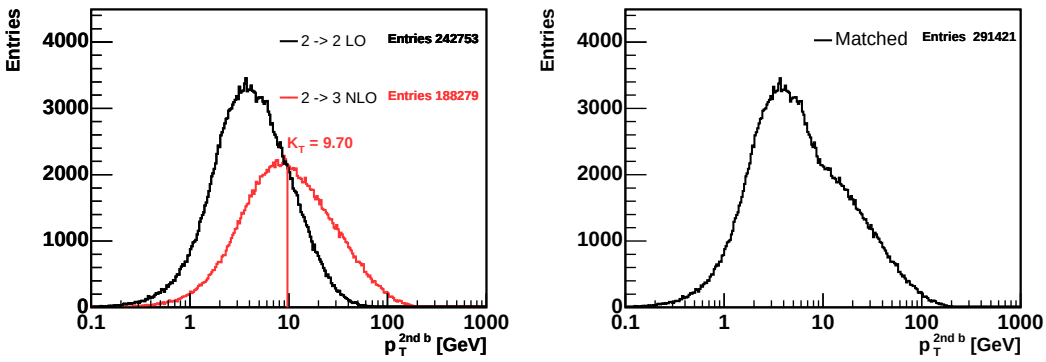

(a) (b)

Figure 3.5: Matching of the $m_t = 175$ GeV/c^2 sample: 2nd-b quark p_T of unmatched MadEvent 2→2 LO and 2→3 NLO samples (a), matched sample (b).

Chapter 4

Validation of the MadEvent Monte Carlo Samples

4.1 ZTOP Software

As mentioned in Chapter 1.3, the ZTOP software, a program to calculate NLO s-channel and t-channel single-top-quark production distributions, is based on the phase space slicing method, namely on a spin-averaged version. Since it provides the possibility to calculate transverse momentum and pseudorapidity distributions within the geometrical acceptance of a given detector, it is very appropriate to verify event samples of MC generators. The method of ZTOP is fully differential and produces final state jet and not parton distributions. This is a consequence of the formalism of the NLO calculations. Instead of flavor-ordered partons one has to compare p_T-ordered jets. Since b quark jet distributions differ from those of light quark jets, ZTOP distinguishes between jets with and without b quark content. This b quark is always the already mentioned 2nd-b quark, because ZTOP does not cover the decay of the top quark. Further contributions to light quark jets may come from initial- or final-state gluon radiation, for instance Figure 1.6. As a result of all these matters, ZTOP produces the following relevant distributions: p_T and η of the top quark at parton level, as well as of the p_T-ordered leading jet and of the 2nd-leading jet. There are separate distributions for jets with or without b quark content.
To produce the NLO distributions, we used ZTOP version 1.0 with the default parameters, except for minor adjustments: the W boson mass was set to 80.42 GeV/c^2, the top quark mass was set to 175 GeV/c^2 and the k_T cone size was set to 0.54, which corresponds to a fixed cone size of 0.4 used by CDF. To get better statistics, the initial number of Vegas iterations and points were set to the values recommended for graphing. The parton density functions were set to CTEQ5M1. Only top (no antitop) quark production was performed. Thus, the cross section was doubled to match the predictions for top and antitop production. Since the antitop distributions in $p\bar{p}$ collisions differ solely by the signs of η, we plot $Q_l \cdot \eta$ distributions when comparing with MadEvent, which contains top and antitop events. Here Q_l is the charge of the lepton coming indirectly from the top quark decay (+1 for top, -1 for antitop quark production in units of the elementary charge).

4.2 Validation

To validate the MadEvent s- and t-channel MC samples by means of the ZTOP calculations, acceptance cuts of $p_T > 15$ GeV and $|\eta| < 2.8$ are applied to the jet distributions of light quark and b quark. These cuts are motivated by the jet definition used in the single-top analysis. No cuts are applied to the top quark, since it further decays before building a jet. In the MadEvent event listing, the top quark is not included, so one has to build its fourvector out of the decay products at parton level, namely the W boson and the 1st-b quark. The MadEvent s- and t-channel top quark distributions are normalized to the total ZTOP cross section of 0.870 pb or 1.985 pb, respectively. These normalizations yield the scales that are used for the normalization of all following s- and t-channel distributions. That means that the jet distributions are also normalized to the inclusive cross section. There is no additional normalization of these distributions.
For all but the top quark distributions, one has to compare p_T-ordered jets, in t-channel with the additional distinction between jets with or without b quark content. The potential 1st-b quark jet from the top decay is not considered in the remainder of this thesis, since ZTOP does not cover this decay. We therefore will assume that the 1st-b quark is well modeled in MadEvent. The differences between the integral of the p_T and $Q_l \cdot \eta$ distributions are due to overflow entries beyond the histogram boundaries.

4.2.1 s-channel Sample

In Figure 4.1 the top quark p_T and $Q_l \cdot \eta$ distributions of MadEvent and ZTOP are shown. The MadEvent top quark p_T is slightly harder than the ZTOP spectrum, in $Q_l \cdot \eta$ the distributions match perfectly.

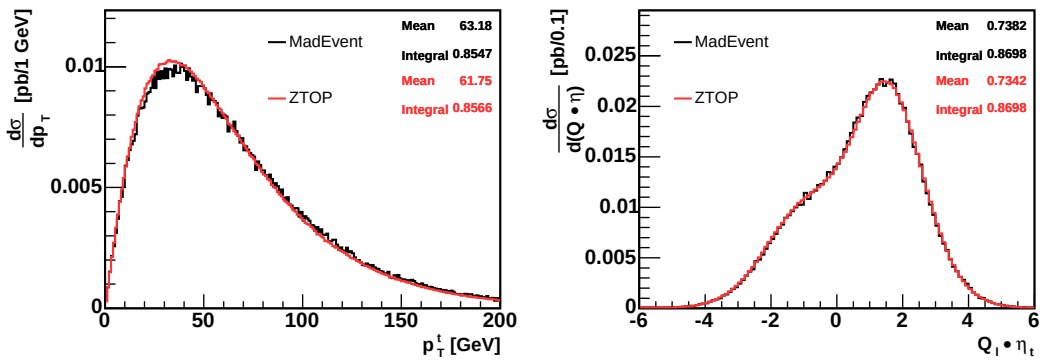

(a) (b)

Figure 4.1: s-channel top quark transverse momentum p_T (a) and lepton charge times top quark pseudorapidity $Q_l \cdot \eta$ (b).

The ZTOP software calculates, that at least one jet (apart from the 1st-b quark jet) should be visible within the detectors acceptance in about 92.8% of all s-channel events. In the majority of events (84.3%) this p_T-leading jet is a 2nd-b quark jet, which is in MadEvent represented by a 2nd-b quark at parton level. Only in 8.5% ZTOP expects a light quark jet, which in the s-channel comes from initial or final state gluon radiation. Since the s-channel MadEvent sample is LO and does not include matrix elements of gluon radiations, this is modeled by the PYTHIA showering and does therefore not appear at parton level. To take this into account we have to leave the simple parton model which serves well for the 2nd-b quark jets and investigate the events at hadron level after the showering. To do that one has to apply a jet clustering to the stable particles to include these contributions. The parameters of the k_T cluster algorithm, used for this purpose, were set to a cone size of 0.54 (equal to the ZTOP cone size) and to a minimum jet energy of 15 GeV, adjusted to the selection cut used on data. Since the clustering was done with all stable particles constructed by PYTHIA except for the lepton and the neutrino from the top decay, the 1st-b quark from the top decay cannot be excluded and will contribute to the number of jets found by the cluster algorithm.
Due to the QCD color conservation implemented in the PYTHIA hadronization process, one cannot unambiguously trace back the jets to the original quarks, so another method to assign the jets to the partons is needed: at least 3 jets per event after the acceptance cuts were required, one for the 1st-b quark, the 2nd-b quark and the light quark jet. With the jets ordered in transverse momentum, we assume that the probability for the gluon radiated light jet to end up in neither the first nor the second jet is high, since both b quarks are rather hard (Figure 4.2 (a)). To get the light quark jet, one has to study the third ordered jet. The distinction, whether or not a jet is a light quark jet, was done by a cut of the ratio of the jet energy coming from B hadrons, thus from b quarks. We consider jets to be light if less than 30% of the jet energy is from particles coming from B hadrons, see Figure 4.2 (b).

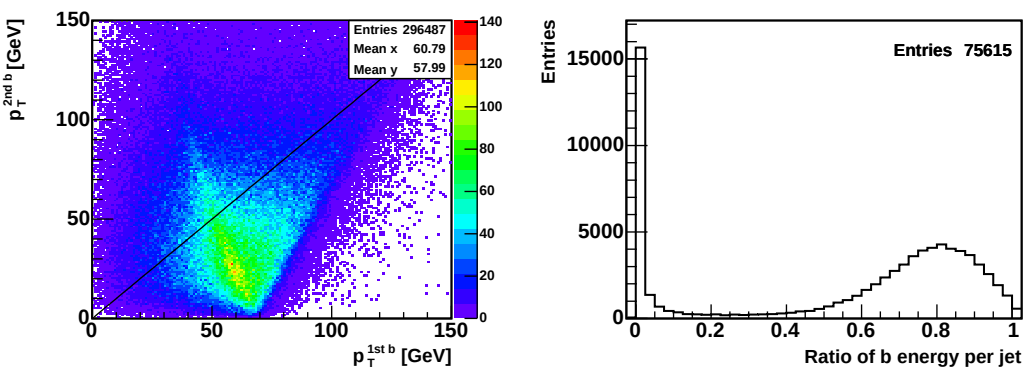

(a) (b)

Figure 4.2: s-channel: p_T of 1st-b quark versus p_T of 2nd-b quark (a) with the line at equal values, ratio of jet energy of clustered particles coming from B hadrons shown for all third ordered jets with any B hadron content (b).

The MadEvent p_T-leading jet (j1) distributions, containing 2nd-b quark jets and a small fraction of clustered light jets, are in good agreement with the ZTOP predictions, as seen in Figure 4.3. There are no differences in the rates, the MadEvent p_T spectrum is slightly too hard. The mean value of p_T is about 3% higher for MadEvent than for ZTOP.

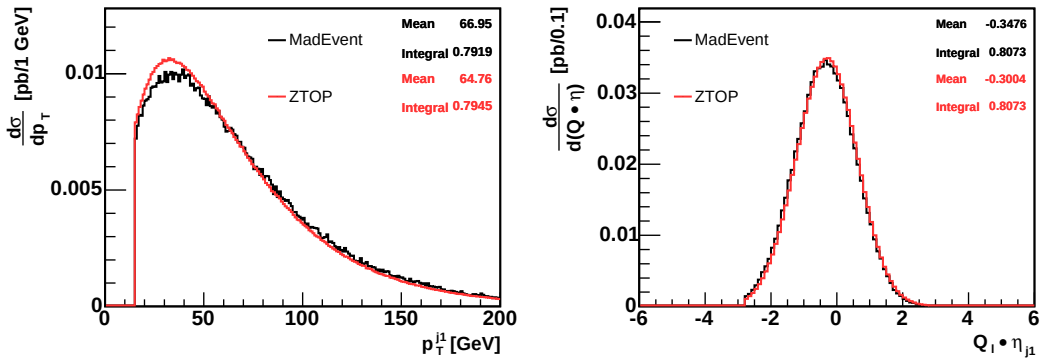

(a) (b)

Figure 4.3: s-channel leading jet (j1) p_T (a) and $Q_l \cdot \eta$ (b). The 1st-b quark from the top decay is excluded from the jet ordering.

The p_T-ordered 2nd-leading jet (j2), appearing in about 23.4% of all events according to ZTOP, is dominated by gluon radiated light jets, in contrast to the leading jets. Only in about 5.4% a 2nd-b quark jet is the 2nd-leading jet. Because of this the MadEvent p_T and $Q_l \cdot \eta$ distributions in Figure 4.4 do not match properly with the ones of ZTOP. The jet clustering of the stable particles does not result in a steeply falling p_T spectrum as predicted by ZTOP. Also in $Q_l \cdot \eta$ MadEvent differs from the theoretical calculations, solely the rates of the 2nd-leading jets comply. Table 4.1 summarizes the relevant s-channel cross sections and fractions.

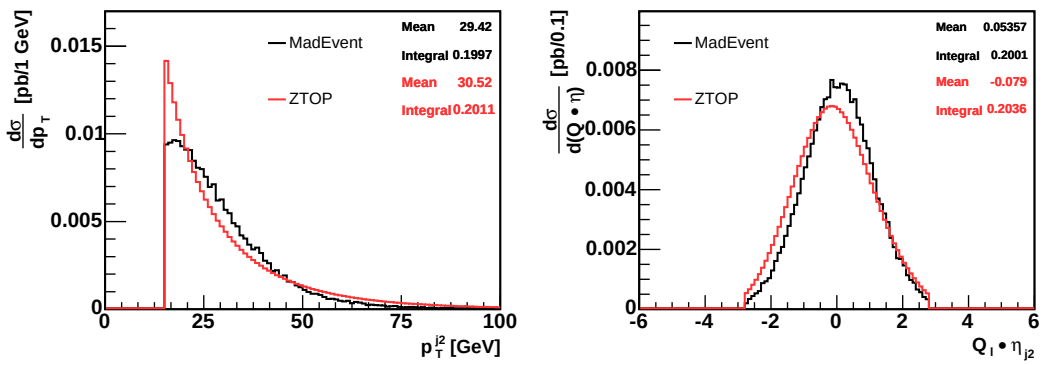

(a) (b)

Figure 4.4: s-channel 2nd-leading jet (j2) p_T (a) and $Q_l \cdot \eta$ (b). The 1st-b quark from the top decay is excluded from the jet ordering.

jet type	ZTOP cross section [pb] and fraction	MadEvent cross section [pb] and fraction
top quark (total cross section)	0.870 100%	0.870 100%
leading b quark jet (b1)	0.733 84.3%	0.799 91.9%
leading light quark jet (q1)	0.074 8.5%	0.008 0.9%
leading jet seen (j1 = b1 + q1)	0.807 92.8%	0.807 92.8%
2nd-leading b quark jet (b2)	0.047 5.4%	0.005 0.6%
2nd-leading light jet (q2)	0.156 18.0%	0.195 22.4%
2nd-leading jet seen (j2 = b2 + q2)	0.204 23.4%	0.200 23.0%

Table 4.1: Summary of all relevant s-channel cross sections and resultant fractions (defined as ratio of the cross sections, with 0.870 pb as denominator). The MadEvent s-channel sample contains a total of 296487 events. The 1st-b quark from the top decay is excluded from the jet ordering.

4.2.2 t-channel Sample

Figure 4.5 shows the comparison of top quark p_T and $Q_l \cdot \eta$ distributions between MadEvent and ZTOP. The t-channel MadEvent top quark distributions are in good agreement with the ZTOP output. The deviation in the mean of the transverse momentum is minor, the MadEvent $Q_l \cdot \eta$ mean value is slightly lower than the one from ZTOP.

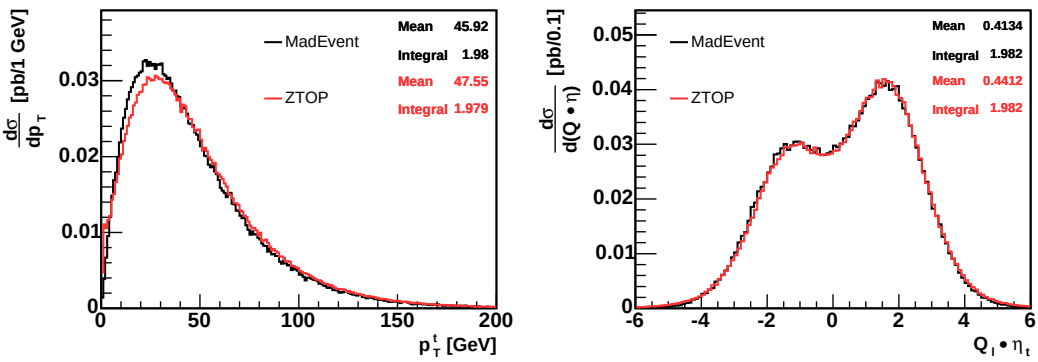

(a) (b)

Figure 4.5: t-channel top quark transverse momentum p_T (a) and lepton charge times top quark pseudorapidity $Q_l \cdot \eta$ (b).

In the case of p_T-leading jets, MadEvent t-channel jets are represented by the corresponding quarks at parton level. The relevant cross sections and event fractions are summarized in Table 4.2. As computed by ZTOP, there should be at least one jet in 81.0% of all events within the detector acceptance cuts. When the 2nd-b quark jet is the p_T-leading jet (b1), which is the case in 10.5% of all events according to ZTOP, MadEvent underestimates this rate by a factor of about 0.90, as shown in Figure 4.6. The falling p_T spectrum and the central $Q_l \cdot \eta$ distribution are reasonably well simulated by MadEvent.

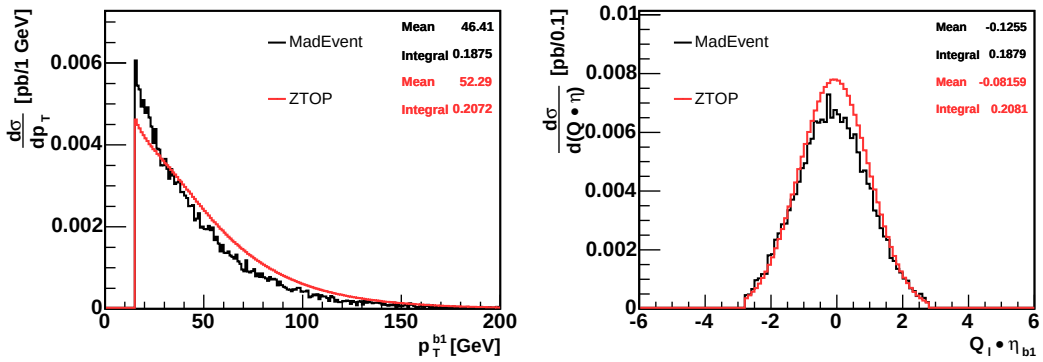

(a) (b)

Figure 4.6: p_T (a) and $Q_l \cdot \eta$ (b) of the t-channel leading b quark jet (b1). The 1st-b quark from the top decay is excluded from the jet ordering.

In the majority of events (70.5% according to ZTOP) the p_T-leading jet will be a light quark jet (q1). In Figure 4.7 one can see that MadEvent reproduces the corresponding distributions very well, the deviations in the mean of p_T as well as of $Q_l \cdot \eta$ are negligible, only the corresponding rate is slightly overestimated by a factor about 1.02.

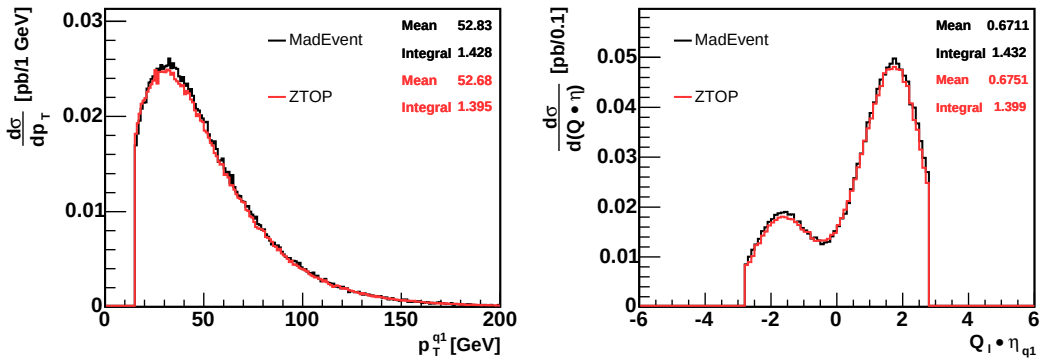

(a) (b)

Figure 4.7: p_T (a) and $Q_l \cdot \eta$ (b) of the t-channel leading light quark jet (q1). The 1st-b quark from the top decay is excluded from the jet ordering.

In 27.1% of all events a second jet (not considering the jet from the top decay as discussed earlier) should be visible within the detector's acceptance. If this p_T-2nd-leading jet is a b quark jet (b2), which implies that in the same event the light quark jet is the p_T-leading jet, one obtains the following distributions of Figure 4.8. Both the falling p_T-spectrum and the slightly asymmetric shape of $Q_l \cdot \eta$ are well modeled by MadEvent, only the rate, i.e. the cross section, is slightly too high by a factor of about 1.09.

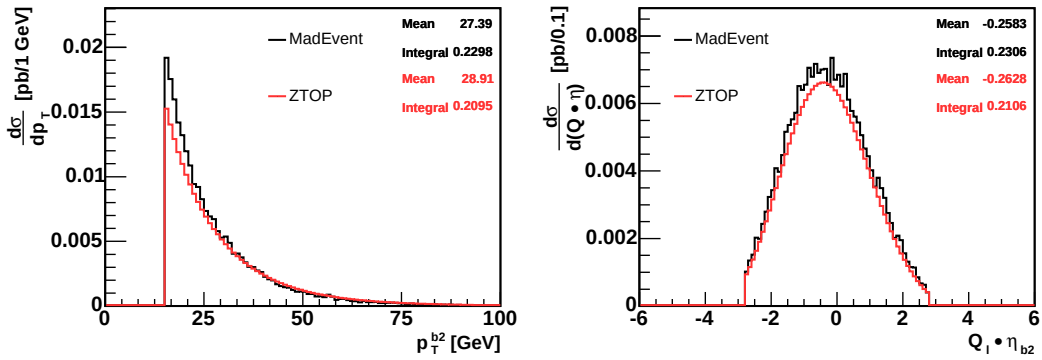

(a) (b)

Figure 4.8: p_T (a) and $Q_l \cdot \eta$ (b) of the t-channel 2nd-leading b quark jet (b2). The 1st-b quark from the top decay is excluded from the jet ordering.

If the p_T-2nd-leading jet is a light quark jet (q2), the MadEvent jet picture represented by the parton level light quark does not agree with the ZTOP predictions. In Figure 4.9 one can observe a big discrepancy in the rate, which is too low by a factor of about 0.29, as well as in the $Q_l \cdot \eta$ shape, which is too far forward.

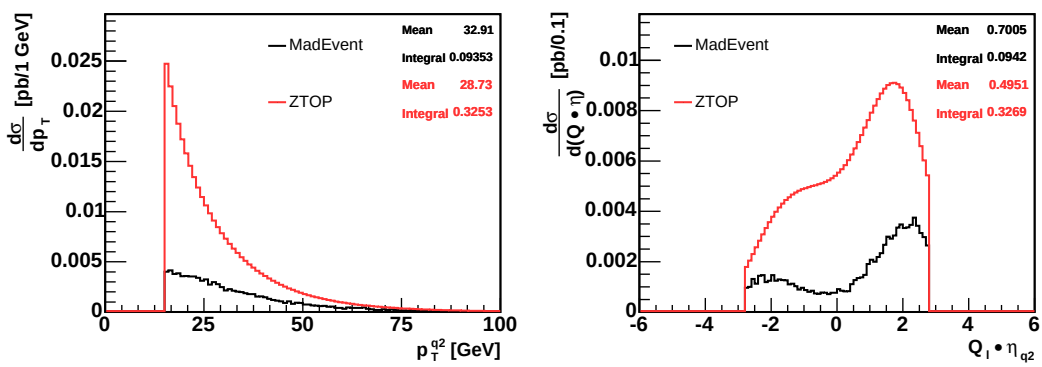

(a) (b)

Figure 4.9: p_T (a) and $Q_l \cdot \eta$ (b) of the t-channel 2nd-leading light quark jet (q2). The 1st-b quark from the top decay is excluded from the jet ordering.

The reason for the bad agreement could be that the matched MadEvent sample does not include all relevant 2→3 NLO matrix elements. We assume that initial state gluon splitting (Figure 1.7 (b)) as well as initial and final state gluon radiations (Figure 1.7 (c) and (d)) may have major contributions to light quark jets, especially to softer ones as considered in the p_T-2nd-leading jets. The contributions to b quark jets should be significantly lower due to the small probability of gluons splitting in $b\bar{b}$ quark pairs.
The same circumstance is discussed in Section 4.2.1, where the s-channel light jets are produced via gluon radiations. Again, a jet clustering of stable particles will be necessary to collect the contributions generated by the PYTHIA showering. In the t-channel case, a different method to assign the jets to the partons is needed: at least 3 jets per event after the acceptance cuts were required, one for the p_T-leading, 2nd-leading and for the 1st-b quark jet respectively. With the jets ordered in transverse momentum, the probability for the 1st-b quark parton to end up in the third jet can be assumed to be low, since the 1st-b quark parton is mostly higher in p_T than both the light quark parton and the 2nd-b quark parton as shown in Figure 4.10 (a).

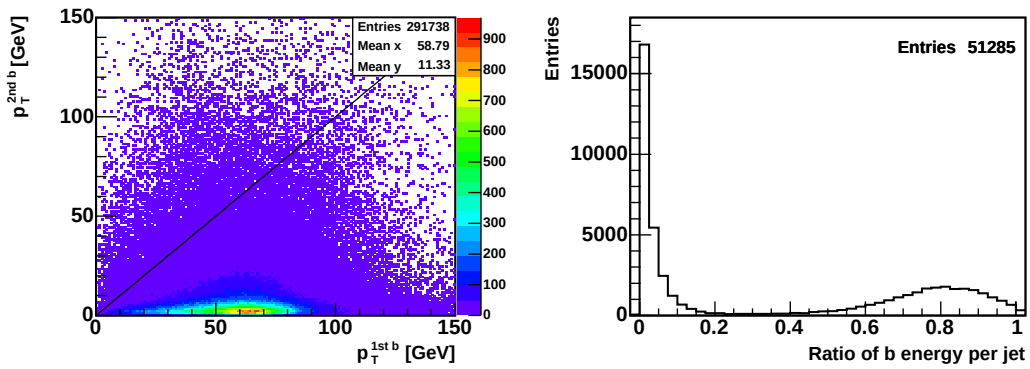

(a) (b)

Figure 4.10: t-channel: p_T of 1st-b quark versus p_T of 2nd-b quark (a) with the line at equal values, ratio of jet energy of clustered particles coming from B hadrons shown for all third ordered jets with any B hadron content (b).

To get the 2nd-leading light quark jet, one has to study the third ordered jet, when there is no 2nd-leading b quark parton in the event. The same distinction as in Section 4.2.1, whether or not a jet is a light quark jet, was used. In Figure 4.10 (b) the corresponding ratio for all jets with any b content is shown. The peak at very small values of the ratio is due to single particles coming from B hadrons, which are clustered into original light quark jets. If the majority of the clustered particles originates from B hadrons, the ratio of b energy per jet accumulates at high values. As already mentioned in Section 4.2.1, we consider jets to be light if less than 30% of the jet energy is from particles coming from B hadrons.

With these jet definitions, the distributions change heavily and a more reasonably agreement of the rates is reached as shown in Figure 4.11. The steeply falling p_T spectrum is not well modeled and the $Q_l \cdot \eta$ distribution has only poor agreement with the ZTOP predictions, since it is far too central. The rate is too high by about a factor of 1.15, but given the fact, that the matching procedure was performed with only two of the four relevant matrix elements, differences in these distributions are to be expected.

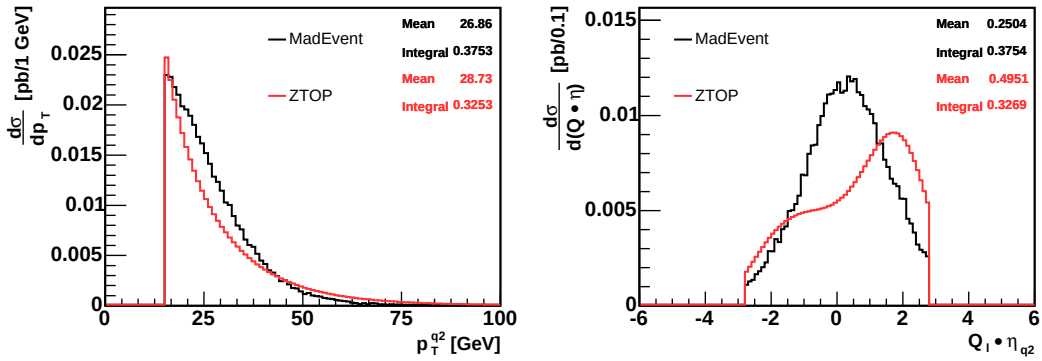

(a) (b)

Figure 4.11: p_T (a) and $Q_l \cdot \eta$ (b) of the clustered 2nd-leading light jet (q2) in the t-channel. The 1st-b quark from the top decay is excluded from the jet ordering.

Modeling the distributions of the 2nd-b quark is the main reason for the MadEvent t-channel matching, performed in Chapter 3. This was done by adjusting the rate of the 2nd-b quark jet to the NLO prediction. The corresponding p_T and $Q_l \cdot \eta$ distributions are shown in Figure 4.12. They are built by the sum of the leading b quark jet (b1) and 2nd-leading b quark jet (b2) distribution. One can certainly state that the matching procedure of the t-channel MadEvent samples works very well.

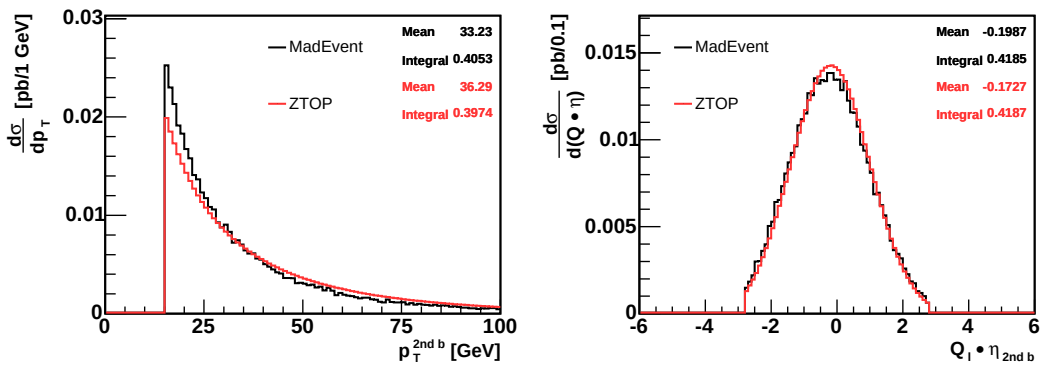

(a) (b)

Figure 4.12: p_T (a) and $Q_l \cdot \eta$ (b) of the matched t-channel 2nd-b jet (2nd b=b1+b2).

jet type	**ZTOP** cross section [pb] and fraction	**MadEvent** cross section [pb] and fraction
top quark (total cross section)	1.985 100%	1.985 100%
leading b quark jet (b1)	0.208 10.5%	0.188 9.5%
leading light quark jet (q1)	1.399 70.5%	1.432 72.2%
leading jet seen (j1 = b1 + q1)	1.607 81.0%	1.620 81.6%
2nd-leading b quark jet (b2)	0.211 10.6%	0.231 11.6%
2nd-leading light jet (q2)	0.327 16.5%	0.375 18.9%
2nd-leading jet seen (j2 = b2 + q2)	0.538 27.1%	0.606 30.5%
2nd-b quark jet (2nd-b = b1 + b2)	0.419 21.1%	0.419 21.1%

Table 4.2: Summary of all relevant t-channel cross sections and resultant fractions (defined as ratio of the cross sections, with 1.985 pb as denominator). The matched MadEvent t-channel sample contains a total of 291738 events. The 1st-b quark from the top decay is excluded from the jet ordering.

Chapter 5

Estimate of Systematic Uncertainty on the MC Model

The underlying concept of estimating the systematic uncertainty is to use the deviations between the ZTOP and the MadEvent variables. By building a ratio-function of ZTOP over MadEvent bin by bin for each variable, one can see in which region MadEvent under- and overestimates the signal. Each event passing the single-top selection cuts gets a scale corresponding to the ratio of its bin. The sum of all scales approximates the corrected acceptance. Half of the arising difference between the corrected and the original acceptance is taken as symmetric systematic uncertainty. Since one has several variables and therefore several ratio-functions per event, an appropriate procedure has to be found to compute an overall scale per event. The applied proceeding is similar to the least-squares-method of weighted average. At this level the correlations between the ratio-functions $r_i(bin) = ZTOP_i(bin)/MadEvent_i(bin)$ are taken into account. The index i stands for one of the N_{var} used variables. A covariance-matrix V_{ij} of all produced ratio-functions $r_i(bin)$ is constructed by running over all N_{ev} events of the full MadEvent sample of s- or t-channel, respectively. For each event n the ratios $r_i(bin_{in})$ of the considered variables i are calculated by taking the content of bin_{in}, the event n is located in:

$$V_{ij} = \frac{S_{ij} - S_i \cdot S_j/N_{ev}}{N_{ev} - 1} \qquad \text{with } S_i = \sum_{n=1}^{N_{ev}} (r_i(bin_{in}) - 1) \tag{5.1}$$

$$\text{and } S_{ij} = \sum_{n=1}^{N_{ev}} (r_i(bin_{in}) - 1) \cdot (r_j(bin_{jn}) - 1) \qquad \text{for } i, j = 1, 2, ...N_{var}.$$

The weight-matrix M_{ij} is obtained by inverting the covariance-matrix: $M_{ij} = V_{ij}^{-1}$ For each event m of all N_{pre} events passing the preselection, a weighted scale s_m is calculated as follows:

$$s_m = \sum_{i=1}^{N_{var}} w_i \cdot r_i(bin_{im}), \tag{5.2}$$

where the weight is given by $w_i = \sum_{j=1}^{N_{var}} M_{ij} / \sum_{k,l=1}^{N_{var}} M_{kl}$

One obtains the corrected acceptance A by summing up all weighted scales s_m:

$$A = \sum_{m=1}^{N_{pre}} s_m \tag{5.3}$$

Since the single-top analysis investigates both the 2- and 3-jet-bin, this method is done for the 2-, 3- and 2+3-jet-bin separately. To take into account the statistical fluctuations, several actions are implemented by creating the ratio-functions. They are exemplarily shown in Figure 5.1: A smoothing of the original (a) t-channel p_T distribution of the leading b jet is conducted (b). To get the long tails of the p_T distributions under control, overflow bins are established in the ratio-functions for p_T higher than 75 GeV or 150 GeV, respectively (c). Under- and overflow bins are also used in the low statistic regions $|\eta| > 4.0$ of the top quark $Q_l \cdot \eta$ distributions. In the case of big unphysical oscillations in the ratio-functions, the affected region is approximated by a fit of a polynomial of low order (d).

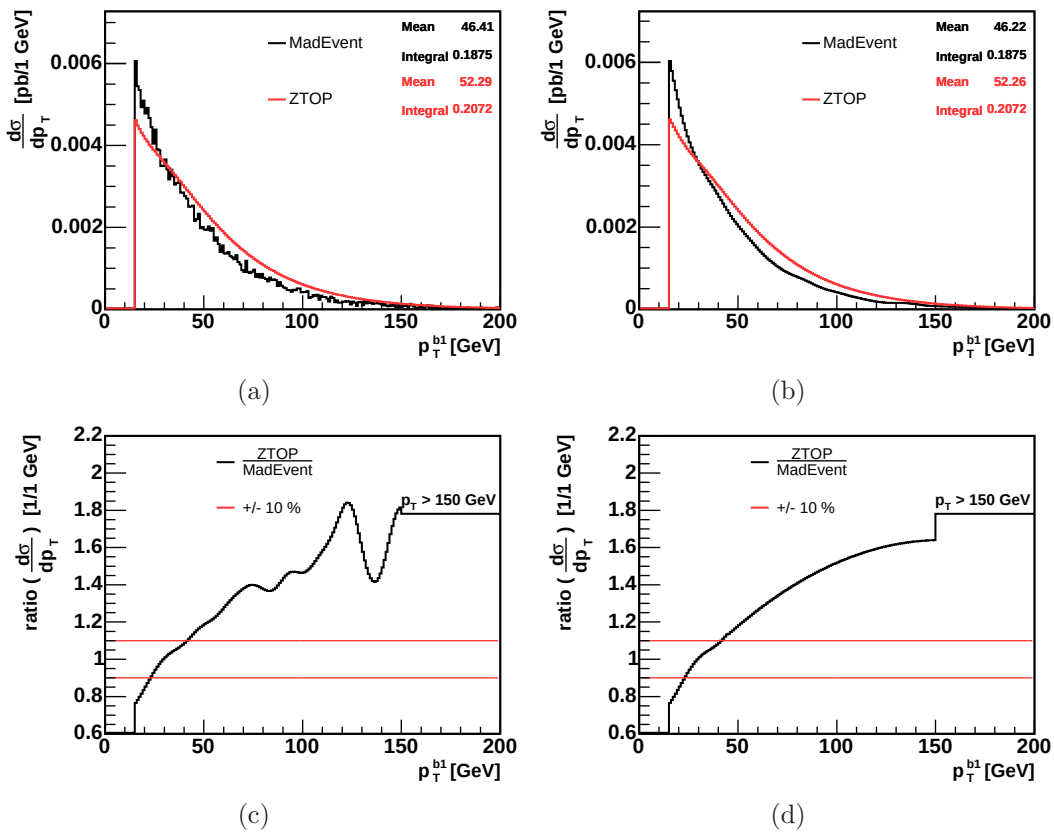

Figure 5.1: Intermediate steps by building the ratio-functions: the original (a) distributions are smoothed (b). Under- and overflow bins are established in the low statistic regions, here $p_T > 150$ GeV, of the ratio-functions (c). Appearing unphysical oscillations are approximated by a fit (d).

5.1 s-channel Estimate

$N_{var} = 6$ variables, validated in Chapter 4.2.1, are used to estimate the s-channel systematic uncertainty: p_T and $Q_l \cdot \eta$ of the top quark, of the p_T-ordered leading jet (j1) and of the 2nd-leading jet (j2). Their ratio-functions are shown in Figure 5.2.

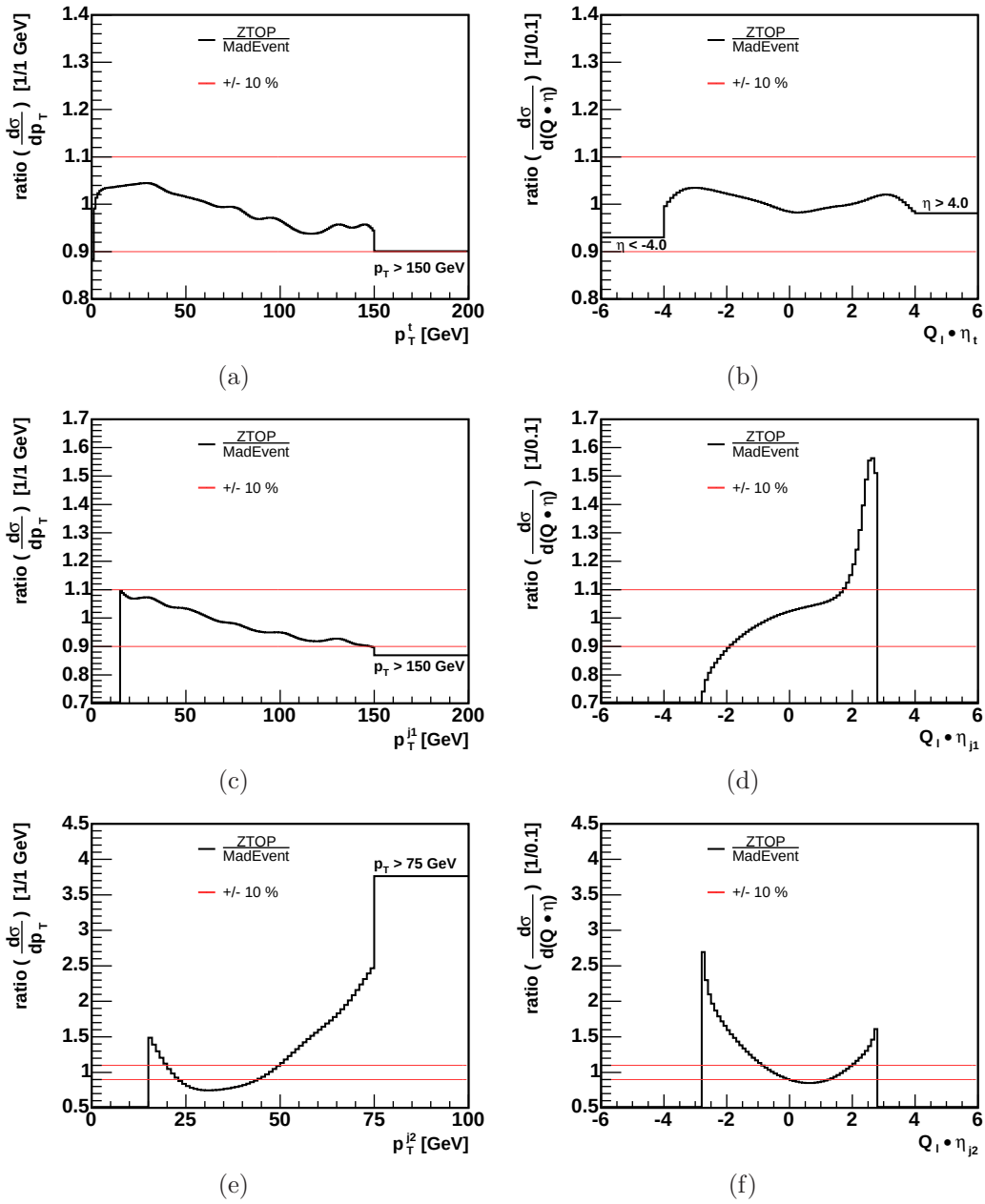

Figure 5.2: Ratio-functions of the s-channel top quark ((a) and (b)), leading jet j1 ((c) and (d)) and 2nd-leading jet j2 ((e) and (f)).

One has to distinguish between three kinds of events at generator level: Those with no jets within the detectors acceptance (labeled: t), those with one jet (tj1) and those with two jets visible (tj1j2). The top quark variables are always included.

For each of these cases a separate weight-matrix of the ratio-functions has to be computed. The corresponding correlation-matrices are shown in Figure 5.3.

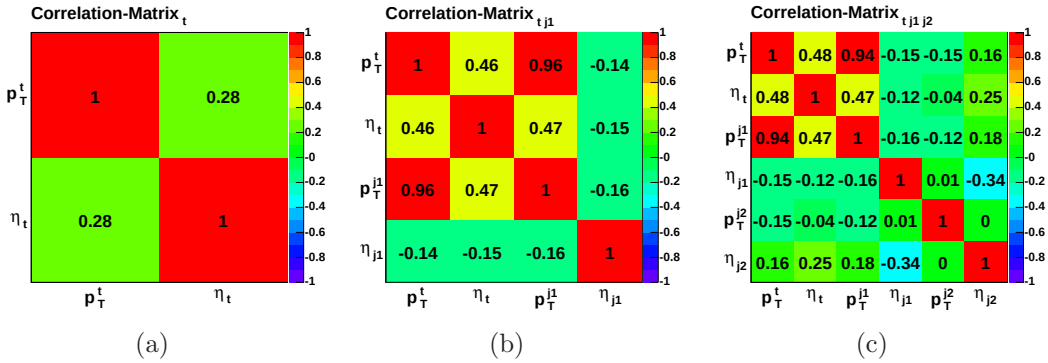

Figure 5.3: s-channel correlation-matrices of the ratio-functions, separate for the subsamples t (a), tj1 (b) and tj1j2 (c).

Depending on the kind of event passing the preselection, the corresponding weight-matrix is used to calculate the weighted scale s_m. As an example, all scales of the preselected events of the 2+3-jet-bin are plotted in Figure 5.4. Table 5.1 specifies the corrected acceptance and its estimated uncertainty for each jet-bin.

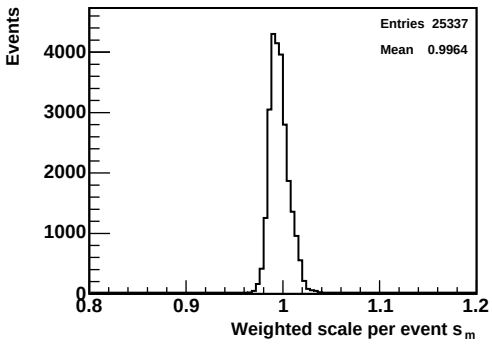

Figure 5.4: Scales of the s-channel events passing the 2+3-jet-bin preselection, the deviation of the mean from 1.0 is only about 0.4%.

	2-Jet-Bin	**3-Jet-Bin**	**2+3-Jet-Bin**
original acceptance	20895.0	4442.0	25337.0
corrected acceptance	20825.7	4419.4	25245.0
correction	-0.33%	-0.51%	-0.36%
estimated uncertainty	$\pm 0.2\%$	$\pm 0.3\%$	$\pm 0.2\%$

Table 5.1: Summary of the s-channel results. The estimated uncertainty is half the absolute value of the difference between original and corrected acceptance. The original acceptance is given as the number of MC events passing the single-top selection.

5.2 t-channel Estimate

For the t-channel, all $N_{var} = 10$ variables validated in Chapter 4.2.2 are considered. In contrast to the s-channel, it is distinguished whether or not a jet has a b quark content to treat the matched 2nd-b quarks separately. The ratio-functions of p_T and $Q_l \cdot \eta$ of the top quark, of the leading b jet b1, of the leading light jet q1, of the 2nd-leading b jet b2 and of the 2nd-leading light jet q2 are shown in Figure 5.5 and 5.6.

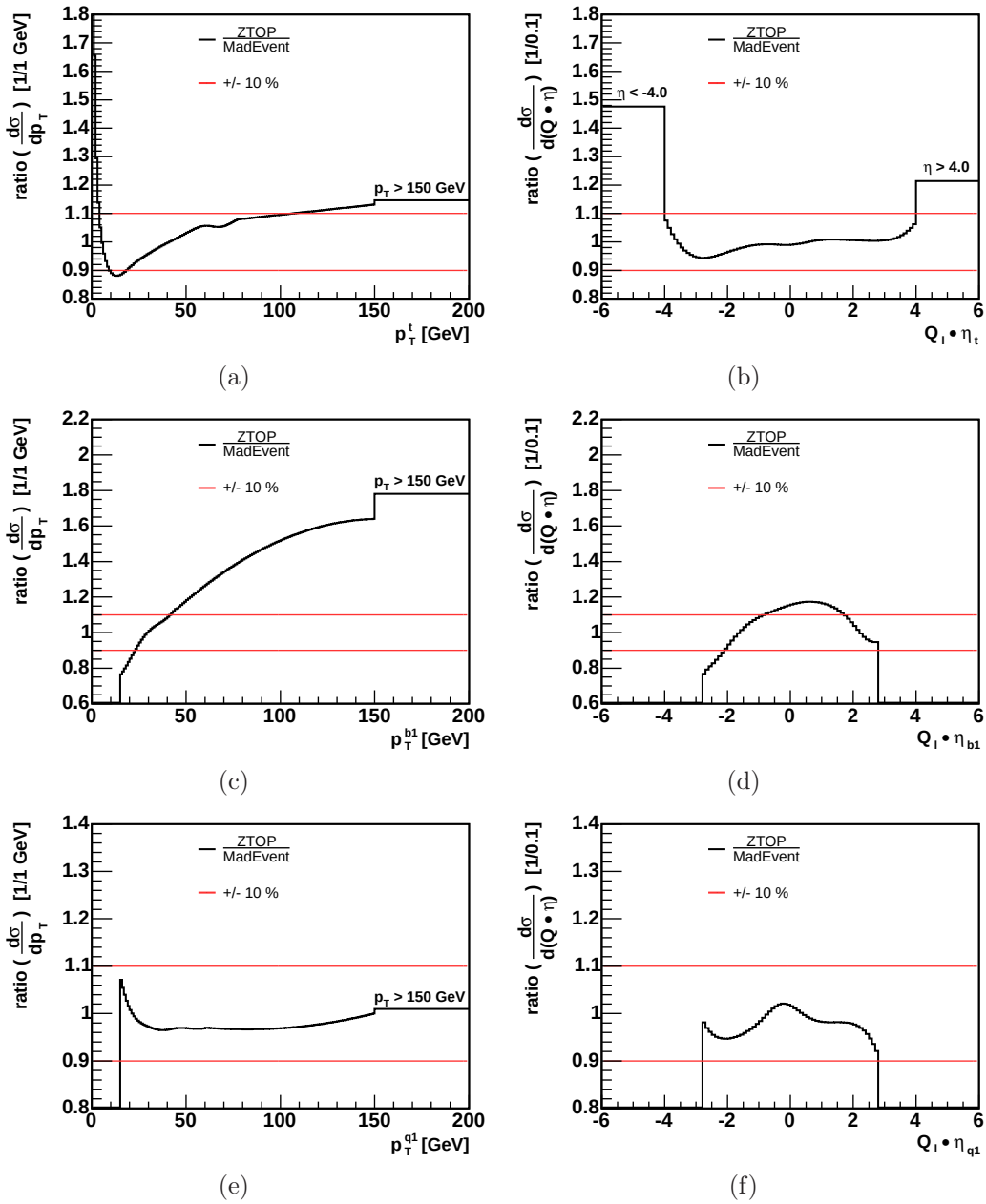

Figure 5.5: Ratio-functions of the t-channel top quark t ((a) and (b)), leading b jet b1 ((c) and (d)) and leading light jet q1 ((e) and (f)).

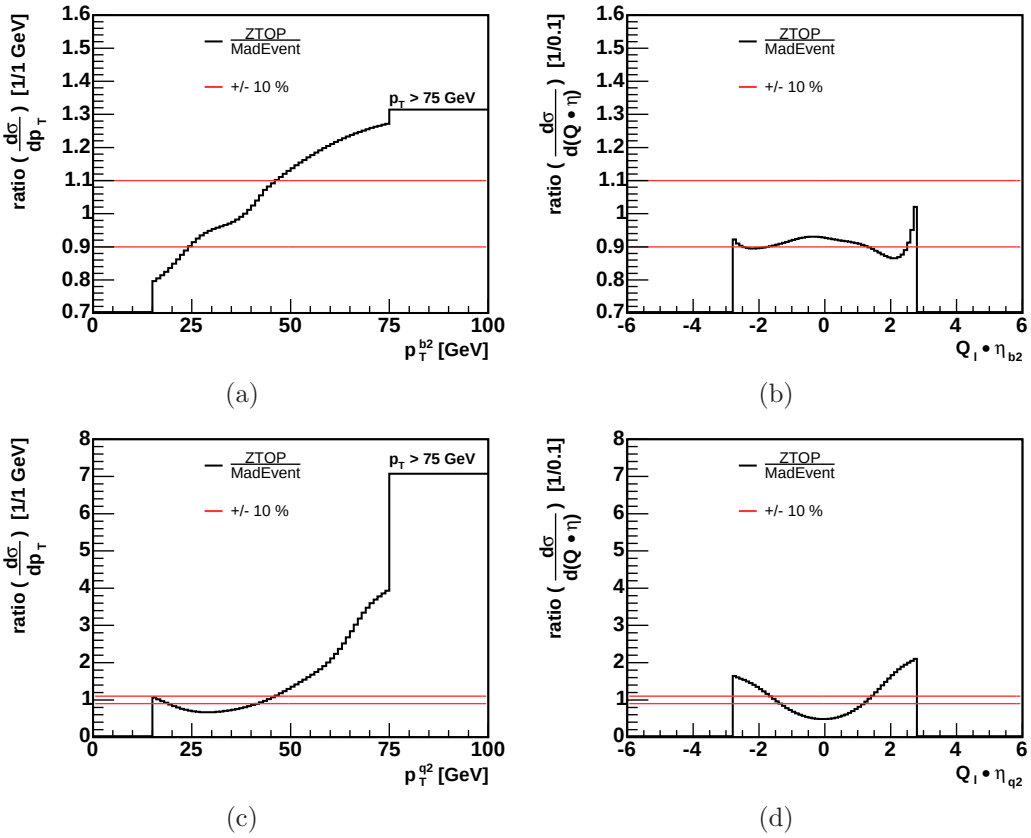

Figure 5.6: Ratio-functions of the t-channel 2nd-leading b jet b2 ((a) and (b)) and 2nd-leading light jet q2 ((c) and (d)).

Due to the flavor discrimination used in the t-channel, one has to deal with 6 different kinds of events: only top (labeled t), top plus b jet (tb1), top plus light jet (tq1), top plus leading b jet plus 2nd-leading light jet (tb1q2), top plus leading light jet plus 2nd-leading b jet (tq1b2) and top plus leading light jet plus 2nd-leading light jet (tq1q2). As discussed for the s-channel, separate weight-matrices are used for each case. The corresponding correlation-matrices are shown in Figure 5.7 and 5.8.

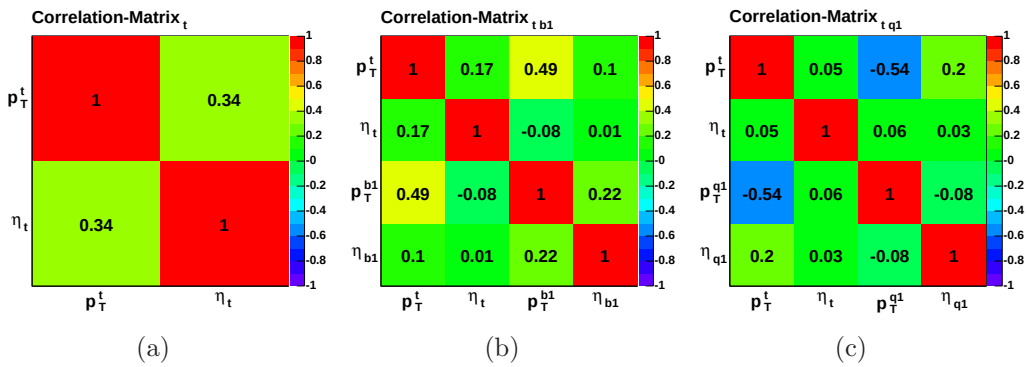

Figure 5.7: t-channel correlation-matrices for the subsamples t (a), tb1 (b) and tq1 (c).

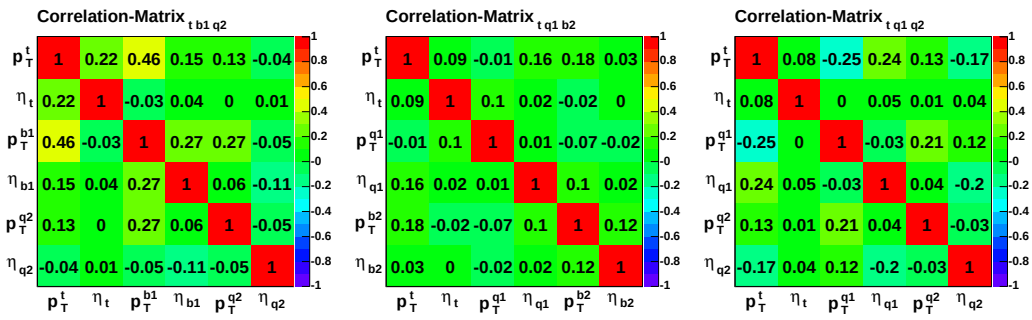

(a) (b) (c)

Figure 5.8: t-channel correlation-matrices for tb1q2 (a), tq1b2 (b) and tq1q2 (c).

In Figure 5.9 (a) the scales of the events passing the 2+3-jet-bin selection are shown. The distribution peaks at about 0.98, a smaller accumulation is located around 1.03. Figure 5.9 (b) and (c) show the frequency of the different kinds of events with a scale smaller and higher than about 1.01. It is clearly visible, that the scale is higher, when a leading b jet is found in the event. This arises from the high values in the ratio-functions (Figure 5.5 (c) and (d)). Table 5.2 lists the corrected acceptance and its estimated uncertainty for each jet-bin.

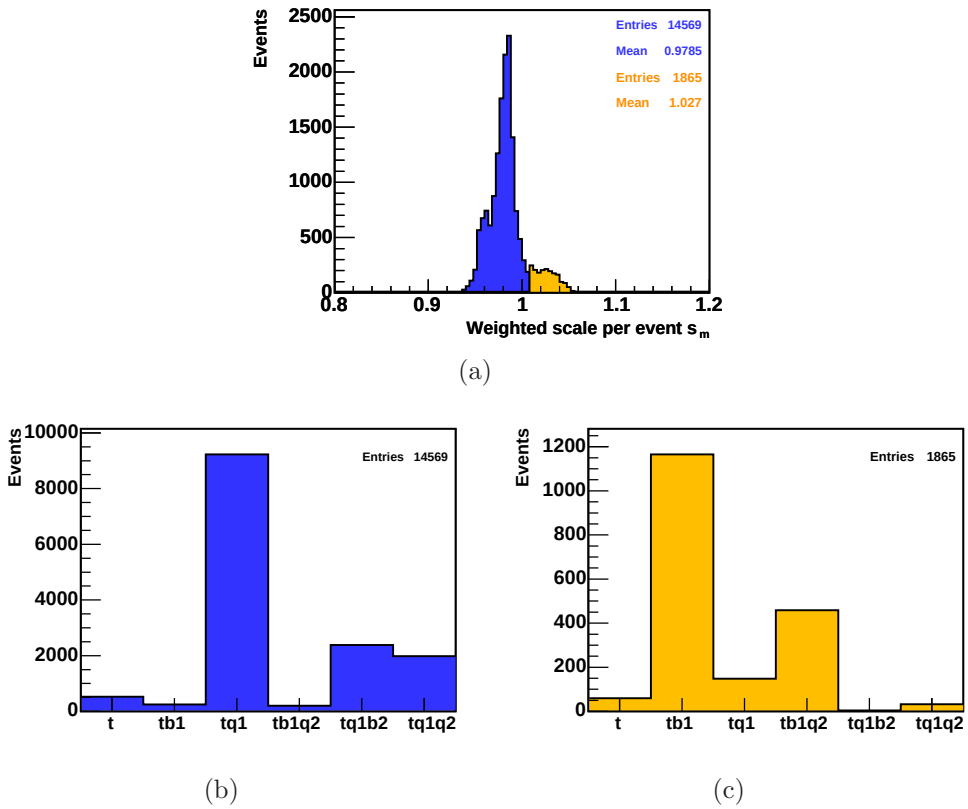

(a)

(b) (c)

Figure 5.9: Scales of events passing the 2+3-jet-bin preselection (a), lower scales are dominated by leading light jets q1 (b), higher scales are dominated by leading b jets b1 (c).

	2-Jet-Bin	**3-Jet-Bin**	**2+3-Jet-Bin**
original acceptance	13204.0	3230.0	16434.0
corrected acceptance	12971.6	3153.4	16128.9
correction	-1.76%	-2.37%	-1.86%
estimated uncertainty	$\pm 0.9\%$	$\pm 1.2\%$	$\pm 0.9\%$

Table 5.2: Summary of the t-channel results. The estimated uncertainty is half the absolute value of the difference between original and corrected acceptance. The original acceptance is given as the number of MC events passing the single-top selection.

Chapter 6

Sensitivity of Single-Top Cross Section Measurement

The direct measurement of the s- and t-channel single-top cross section is an appropriate tool for the accurate determination of the CKM-matrix element V_{tb}. The latest single-top analysis by DØ [8] with an integrated luminosity of 230 pb^{-1} could only set upper limits on s- and t-channel cross section of 6.4 pb and 5.0 pb (95 % C.L.), respectively. At present, the CDF II-experiment has collected data up to 1 fb^{-1} of integrated luminosity. Thus the observation of the single-top production mechanism and the subsequent cross section measurement come into reach.
In the following, a new method for measuring both relevant cross sections is introduced. Two independent neural networks (NN) for s- and t-channel provide the opportunity to determine both values simultaneously. A sensitivity study of the single-top cross section measurement is done assuming an integrated luminosity of 1 fb^{-1}.

In order to estimate the *a priori* sensitivity presuming a scenario of Standard Model single-top production with a s- and t-channel cross section of 0.88 ± 0.11 pb and 1.98 ± 0.25 pb, CDF pseudo experiments are performed. A Poisson distributed random number according to the number of SM expected events for the 2-jet and 3-jet subsample is thrown. The resulting numbers are the events obtained for the signal and background processes. For each event a second random number is drawn according to the probability density assigned to the corresponding NN output template of the 2-jet-bin and 3-jet-bin, respectively. Those templates are obtained by Monte Carlo studies. By this procedure, each pseudo event is assigned to an output value of both the s- and t-channel NN. All these events are accumulated for a pseudo data set corresponding to an integrated luminosity of 1 fb^{-1}.
To calculate the cross sections a fit of a likelihood function to the pseudo data is performed. Here the likelihood function is constructed in the absence of systematic uncertainties, only statistical uncertainties are included.
This pseudo experiment procedure is repeated 10000 times. The widths of the obtained distributions of both the s- and t-channel cross sections determine the estimates for the *a priori* sensitivity of the given scenario.

6.1 Single-Top Preselection

The s- and t-channel MC samples used in this sensitivity study were generated by MadEvent. The top quark mass was set to 178 GeV/c^2, corresponding to the still valid world average. A matching of the t-channel sample was conducted as described in Chapter 3.1. Both signal samples and all relevant background samples passed the detector simulation and production of the CDF offline software. The reconstructed events were converted by TopFind, linked against CDF software release 5.3.3_nt, to produce TopNtuples, the standard data format of the CDF top physics group. Table 6.1 gives an overview on the MC signal and background samples used for the NN training and the calculation of the NN output templates.

Process	**Sample**	N
t-channel matched	mtopta+ua_match	200290
s-channel	mtopya	195928
$t\bar{t}$	ttopel	1150043
WW, WZ, ZZ	wtop1w, wtop1z, ztopcz	1242241
Z$\rightarrow \tau\tau$	ztop1i, ztop4i, ztop5i	3538885
$Wb\bar{b} + 0p$ $(W \rightarrow e/\mu + \nu)$	atopub, atopwb	444375
$Wb\bar{b} + 1p$ $(W \rightarrow e/\mu + \nu)$	atopvb, atopib	443030
$Wc\bar{c} + 0p$ $(W \rightarrow e/\mu + \nu)$	atoprb, atopkb	528966
$Wc\bar{c} + 1p$ $(W \rightarrow e/\mu + \nu)$	atopsb, atoplb	519023
$Wc + 1p$ $(W \rightarrow e + \nu)$	atopic	280381
mistags	atop5a, atop6a, atopdb, atopeb, atop8t	1193572

Table 6.1: Monte Carlo signal and background samples and their corresponding numbers of events N used in this study.

The calculation of a production cross section σ is based on the following formula:

$$\sigma = \frac{N_{signal}}{\epsilon_{evt} \cdot \int \mathcal{L} \text{ dt}} \ , \tag{6.1}$$

where N_{signal} is the number of observed signal events. ϵ_{evt} is the event detection efficiency, which is the average probability of a signal event to be detected. $\int \mathcal{L}$ dt is the integrated luminosity of the data taken by the experiment.
Since the goal of this study is to estimate the sensitivity of a cross section measurement derived from MC studies and pseudo experiments, no data is taken into account. The purpose of the MC studies is to calculate the number of SM predicted signal and background events, respectively. For the signal, equation (6.1) takes the form:

$$N_{signal}^{predict} = \sigma_{signal}^{theo} \cdot \epsilon_{evt} \cdot \int \mathcal{L} \text{ dt} \tag{6.2}$$

Here, σ_{signal}^{theo} is the theoretical calculated SM cross section of the signal. To calculate the number of expected events for the different background processes, corresponding equations are used. The event detection efficiency can be decomposed into four factors:

$$\epsilon_{evt} = \epsilon_{evt}^{MC} \cdot \epsilon_{BR} \cdot \epsilon_{corr} \cdot \epsilon_{trig} \ , \tag{6.3}$$

where ϵ_{trig} is the trigger efficiency and ϵ_{corr} is a correction factor which takes into account the difference between simulated and data events and thereby gives a measure of how well the MC simulation models the detector. Since in some samples the W boson was only allowed to decay into leptons ($W \rightarrow e/\mu/\tau + \nu$), one corrects for this by a branching ratio factor ϵ_{BR}. Using the reconstructed events from the MC samples listed in Table 6.1, one obtains the event detection efficiency ϵ_{evt}^{MC} for Monte Carlo.
This is done by applying all selection and identification cuts of the CDF single-top analysis to the MC events. This preselection corresponds to the standard cuts of the CDF top physics group for lepton+jets analyses [37]. Several requirements to the measured properties of the reconstructed events like number of tight leptons, missing transverse energy because of neutrinos, number of secondary vertices due to long-living B hadrons and so on have to be fulfilled.

The determination of the event detection efficiencies ϵ_{evt} for all relevant signal and background processes is done in reference [38]. Table 6.2 summarizes the number of events of the signal and background MC samples passing the preselection cuts for the 2-jet-bin and 3-jet-bin, respectively.

Process	N **2-jet-bin**	N **3-jet-bin**
t-channel	10516	2345
s-channel	15304	3324
$t\bar{t}$	12756	29819
WW, WZ, ZZ	2194	600
Z$\rightarrow \tau\tau$	629	202
$Wb\bar{b} + 0p$ ($W \rightarrow e/\mu + \nu$)	5184	(704)
$Wb\bar{b} + 1p$ ($W \rightarrow e/\mu + \nu$)	(10456)	3011
$Wc\bar{c} + 0p$ ($W \rightarrow e/\mu + \nu$)	1262	(196)
$Wc\bar{c} + 1p$ ($W \rightarrow e/\mu + \nu$)	(2800)	827
$Wc + 1p$ ($W \rightarrow e + \nu$)	1389	316
mistags	1131	438

Table 6.2: Number of events N of the signal and background MC samples passing the preselection cuts. Numbers in brackets denote samples, which do not belong to that jet-bin.

The resulting numbers of expected signal and background events for an integrated luminosity of 1 fb^{-1} are listed in Table 6.3:

Process	$N^{predict}$ **2-jet-bin**	$N^{predict}$ **3-jet-bin**
t-channel	27.2	6.1
s-channel	18.4	4.0
$t\bar{t}$	61.2	143.2
WW, WZ, ZZ	16.7	4.5
Z$\rightarrow \tau\tau$	7.1	2.8
$Wb\bar{b}$	251.9	64.4
$Wc\bar{c}$	91.9	28.8
Wc	99.7	19.7
mistags	169.2	58.8
Sum	743.3	332.3

Table 6.3: Number of expected events $N^{predict}$ of the signal and background MC samples passing the preselection cuts. This prediction corresponds to an integrated luminosity of 1 fb^{-1}.

6.2 Neural Networks

In this study we benefit from the multivariate method of artificial neural networks to combine several variables into one test statistic which discriminates between signal and background. The neural network used is the NeuroBayes® package [39] provided by the company Phi-T. NeuroBayes® combines a three-layer feed forward neural network as seen in Figure 6.1 (a) with a complex robust preprocessing of the input variables. Bayesian regularization techniques are used for the training process. There is one input node for each input variable plus one bias node. The number of nodes in the hidden layer can be freely chosen by the user. There is one output node which gives a continuous output in the interval [-1,1].
The nodes of two consecutive layers are connected with variable weights. For each node j, a biased weighted sum of the values of the previous layer x_i is calculated

$$a_j(\mathbf{x}) = \sum_i \omega_i x_i + \mu_{0,j} \tag{6.4}$$

and passed to the transfer function which gives the output of the node. The bias $\mu_{0,j}$, which is calculated for each input, implements the thresholds of the several nodes: if the input to a node is larger than its threshold, the node will send an input to the next layer. The output of each node is determined by a transformed sigmoid function

$$S(\mathbf{x}) = \frac{2}{1 + e^{-a(\mathbf{x})}} - 1 \tag{6.5}$$

which gives an output of -1 for background and +1 for signal.

As can be seen in Figure 6.1 (b), the sigmoid function is only sensitive to a relatively small range about zero. By this transformation, the interval $]-\infty, \infty[$ is mapped to the interval [-1,+1]. For very large ($x \to \infty$) or very small ($x \to -\infty$) values, a saturation effect is reached. The bias mentioned above shifts the mean of the input data distribution to the linear part of the sigmoid function.

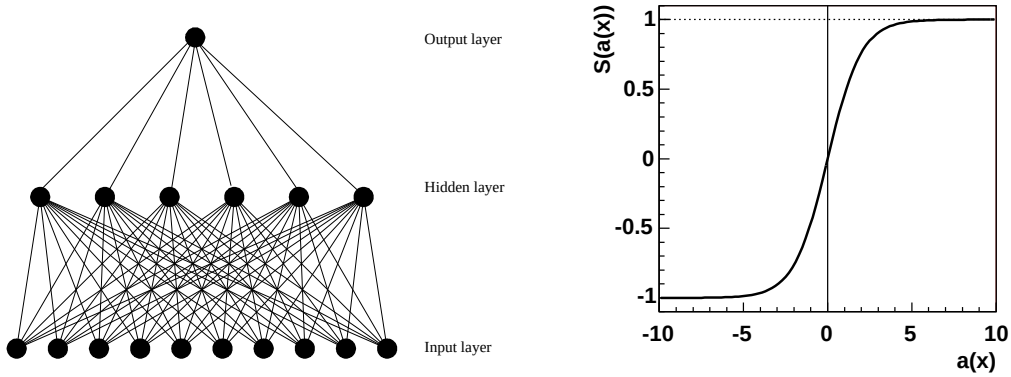

(a) (b)

Figure 6.1: The geometry of a 3 layer neural network (a) and the NeuroBayes® sigmoid function (b) given by formula (6.5).

The output of the neural network for output node k is calculated by

$$o_k = S(\sum_{j=0}^{M} \omega_{kj}^{(2)} \cdot S(\sum_{i=0}^{d} \omega_{ji}^{(1)} x_i + \mu_{0,j})) \tag{6.6}$$

where d is the number of input and M the number of hidden nodes. $\omega_{ji}^{(1)}$ denotes the weights from the input to the hidden layer, $\omega_{kj}^{(2)}$ the weights from the hidden to the output layer. $\mu_{0,j}$ is the weight that connects the bias node with the hidden nodes.

The training of the neural network is done by minimizing the deviation between the true output and the one calculated by using the actual weights. The error function minimized in this neural network is the entropy error function, which is essentially given by the sum of the logarithms of the output values. The aim of the training of the neural network is to find the minimum in the multidimensional structure of the error function with many peaks and valleys. As this task can be difficult to solve, the training process is done by the combined method of gradient descent and backpropagation. The neural network is trained with regularization techniques to improve generalization performance and to avoid overtraining. During the training process, weights and nodes whose significance is below a certain threshold are pruned away. This reduces the number of free parameters and hence improves the signal–to–noise ratio by removing the cause of the noise. This leads again to an improved generalization ability.

For this study, the training of the used networks is done with MC signal and background samples mixed with ratios close to the prediction of the preselection. We have four different networks due to the 2-jet- and 3-jet-bin subsamples, in which we separately train for s- and t-channel signal, respectively. In the training of an s-channel network, the t-channel events are treated as background and vice versa, although this is negligible in our case.

To find the optimal starting point for minimizing the error function, the input variables are preprocessed. This preprocessing is done in a completely automatic way. To care for extreme outliers, the input distributions are equalized to lie between -1 and 1. Those flattened distributions are then converted into a Gaussian distribution, centered at zero with standard deviation 1. This avoids saturation of the nodes due to the above mentioned shape of the activation function in Figure 6.1. After this transformation, the input variables are linearly decorrelated diagonalizing and rotating the covariance matrix into a unit matrix. This unit matrix is again rotated until one variable includes the complete linear correlation to the target and all other correlations are zero.
The above mentioned transformation to a Gaussian distribution may be altered by individual variable preprocessing like fitting the flattened distribution with a spline if this is considered to be sensible. In addition, discrete variables can be treated as members of classes. The preprocessing of those kinds of variables can also deal with a certain order of values if this is important, e.g. the number of jets in an event.
The preprocessing is also able to deal with variables that are not given for every event by assigning the missing values to a δ–function. It is important to mention that the preprocessed input variables do not have any physical meaning, unlike the original ones.

The significances of the training variables are determined automatically during the preprocessing in NeuroBayes®. This is done by removing each variable one after another and check their correlations to the target. This correlation as well as the size of the training sample determine the training significance of each variable. After the preprocessing process, it is possible to cut on the significance to take only variables into account that include enough information that is not already incorporated by other variables.

In this study, the significance cut to the input variables is not applied, since the optimization of these networks is not yet completed. Thus, more than 40 variables are used as input. Some of the most discriminating variables are shown in Figure 6.2 and 6.3.

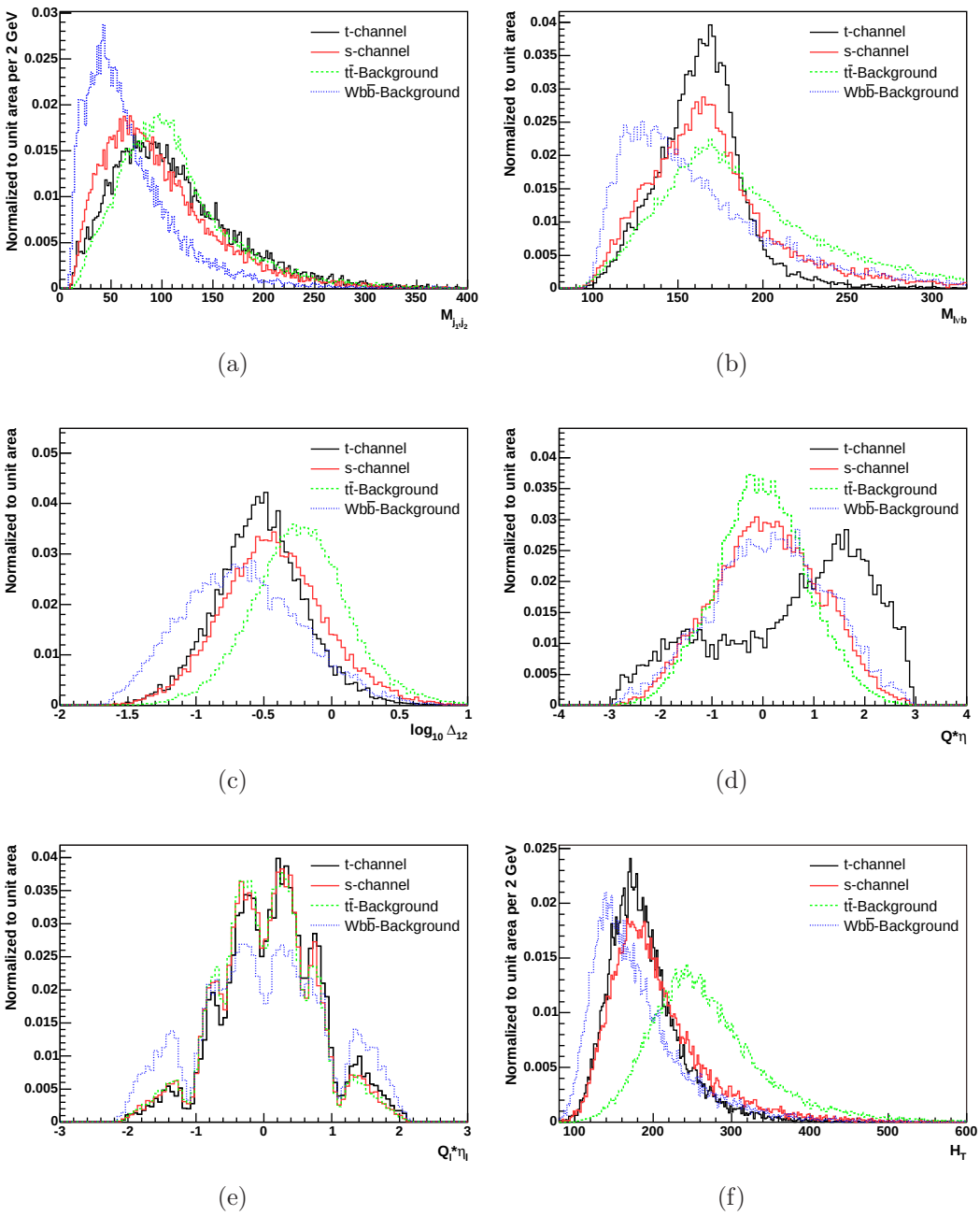

Figure 6.2: Some of the input variables for the neural net: the invariant mass of the two leading jets (a), the reconstructed top mass (b), the logarithm of Δ_{12}, calculated by the K_T jet clustering algorithm (c), the charge of the lepton times pseudorapidity of the leading light jet (d), the charge times pseudorapidity of the lepton (e) and the scalar sum of all transverse momenta in the event (f).

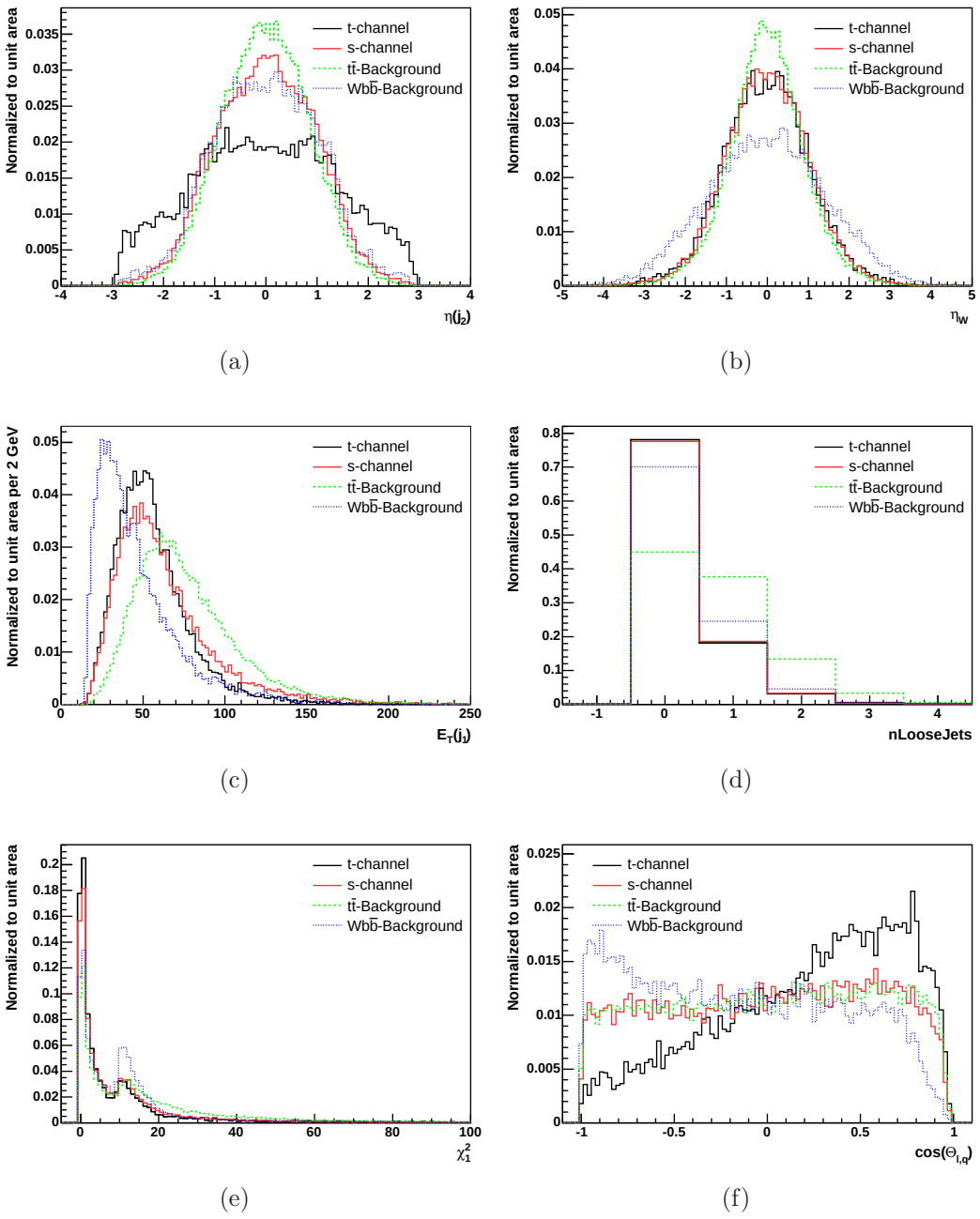

Figure 6.3: Some of the input variables for the neural net: the pseudorapidity of the second leading jet (a), the pseudorapidity of the W boson (b), the transverse energy of the leading jet (c), the number of loose jets in the event (d), the best χ^2 of the Kinematic Fitter for top reconstruction (e) and the cosine of the angle between the lepton and the light jet in the top rest frame (f).

6.3 Templates for Signal and Background

For performing pseudo experiments, template histograms for signal and background must be determined. This has to be done separately for each jet-bin. The background MC events are mixed with the fraction close to the expected ratio. Those events which pass the preselection cuts are fed into both the s- and t-channel neural net. The output of the nets for each sample is the basis of the corresponding template. As a matter of course, one template for each signal channel is constructed. For the background, the proceeding is different. The $t\bar{t}$ sample also obtains its own template. Depending on the deviation between the output of the other background samples, one has to choose which of them would fit into a combined template. Figure 6.4 shows the output of the s- (a) and t-channel (b) NN for different background samples in the 2-jet-bin.

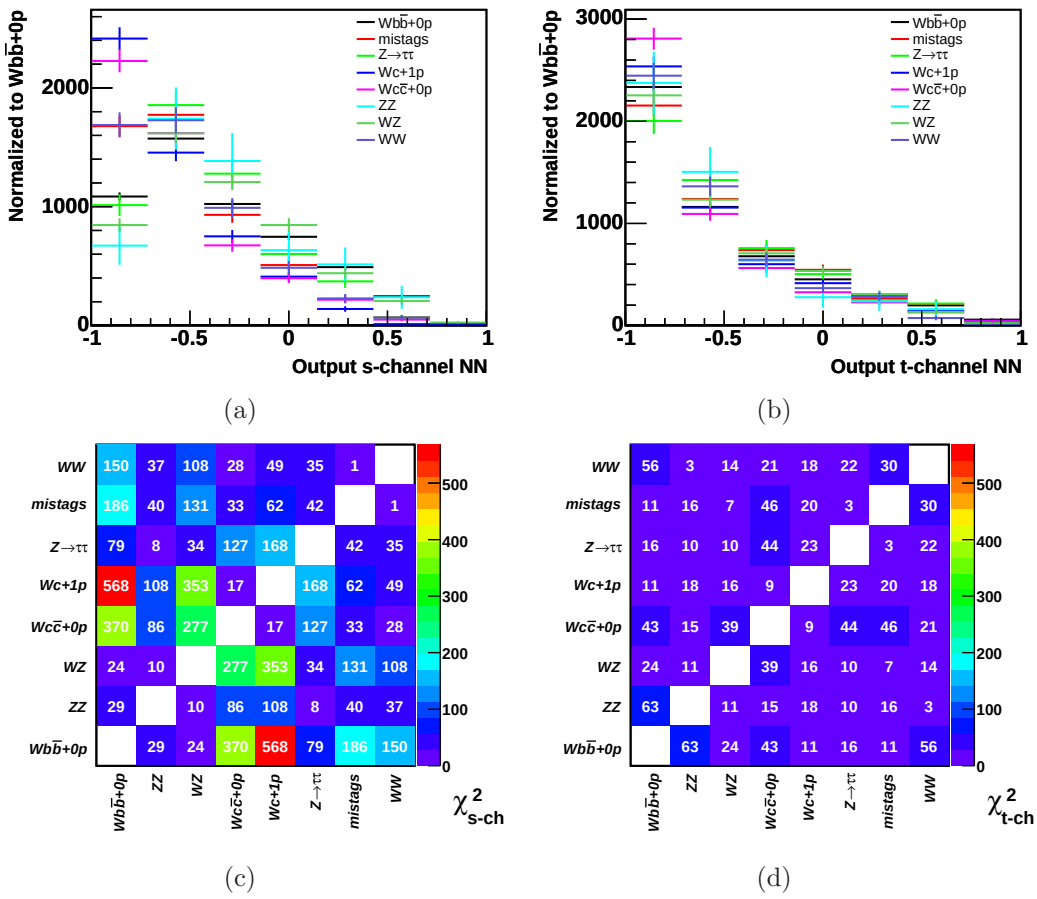

Figure 6.4: 2-jet-bin NN Output of background.

It is obvious, that especially in the output of the s-channel NN the $Wc\bar{c}$ and Wc samples differ from the others. By looking at the the χ^2 between all samples in Figure 6.4 (c) and (d), this is confirmed, only those two have values greater than 200.

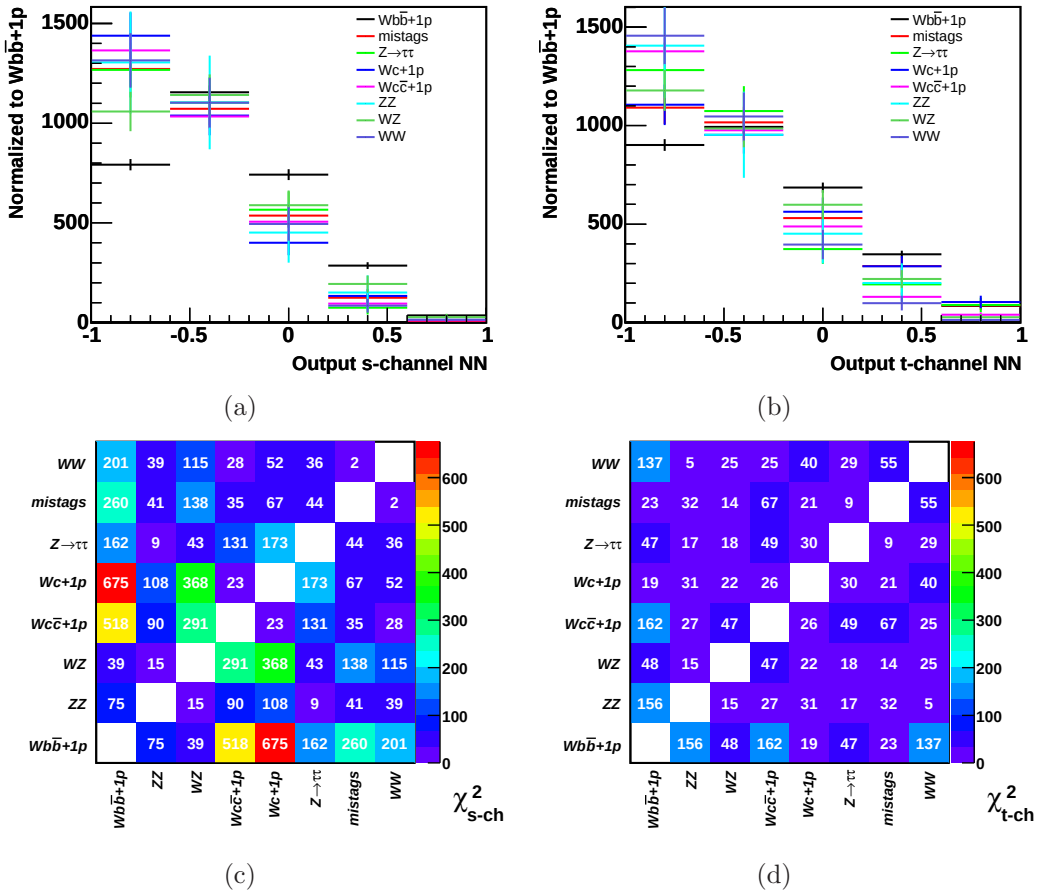

Figure 6.5: 3-jet-bin NN Output of background.

The same is valid for the 3-jet-bin as seen in Figure 6.5. Thus, we decide to establish a charm background template, containing the $Wc\bar{c}$ and Wc samples, and another non-charm template with all remaining backgrounds.

The procedure for constructing the templates is the following. For the 2-jet sub-sample we expect to have about 740 events passing the preselection and about 330 events in the 3-jet-bin (see Table 6.3). Since we want to have about 15 events per bin in the 2D histogram of t- vs. s-channel NN output presuming flat distributions, we choose 7 and 5 output bins for each net in the 2-jet- and 3-jet-bin, respectively. By feeding all MC events of each signal sample (s- and t-channel) and background sample ($t\bar{t}$, charm, non-charm) passing the preselection into both neural nets, we obtain separate 2D output templates. Those distributions get normalized to their expected number of events for an integrated luminosity of 1 fb^{-1} (Table 6.3). For technical reasons, the likelihood fit program can only deal with 1D histograms. The required 1D templates are extracted from the 2D histograms bin by bin.

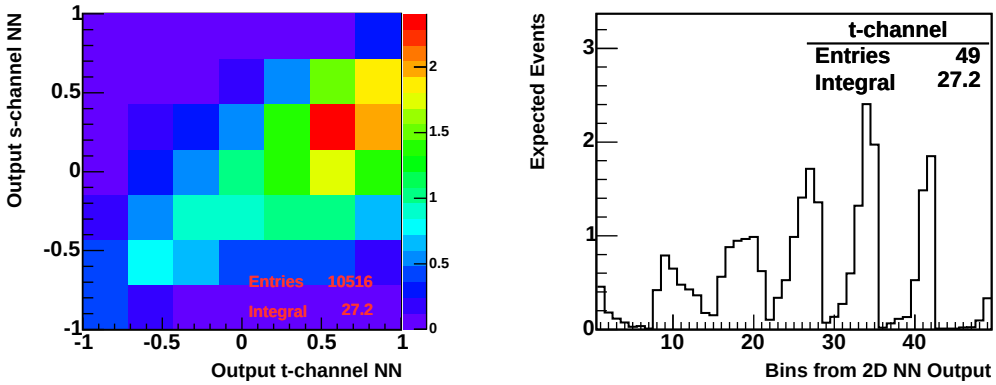

(a) (b)

Figure 6.6: 2-jet-bin 2D NN Output (a) and 1D template (b) of t-channel.

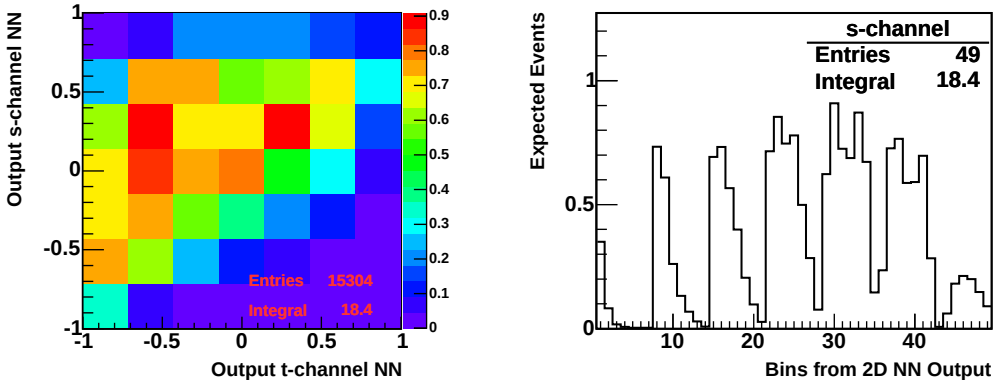

(a) (b)

Figure 6.7: 2-jet-bin 2D NN Output (a) and 1D template (b) of s-channel.

Figure 6.6 (a) shows the 2D NN output for the t-channel sample in the 2-jet-bin. The entries are enriched to x-values near +1, so the t-channel NN is able to identify those entries as signal-like. Even the s-channel NN can do so, as visible in enriched y-values to +1. Figure 6.6 (b) depicts the corresponding 1D template, extracted bin by bin from the 2D NN output histogram.

The 2D NN output for the s-channel sample is seen in Figure 6.7 (a). Here the t-channel NN can not clearly assign all entries to signal events, but the s-channel NN achieves that, even though it is not as effective as the t-channel NN in Figure 6.6 (a).

Figure 6.8 shows the NN outputs for all background samples in the 2-jet-bin. It is clearly visible, that both neural nets are successful in identifying the events as background-like. Nevertheless, there are events which accumulate in the signal regions of the NN output.

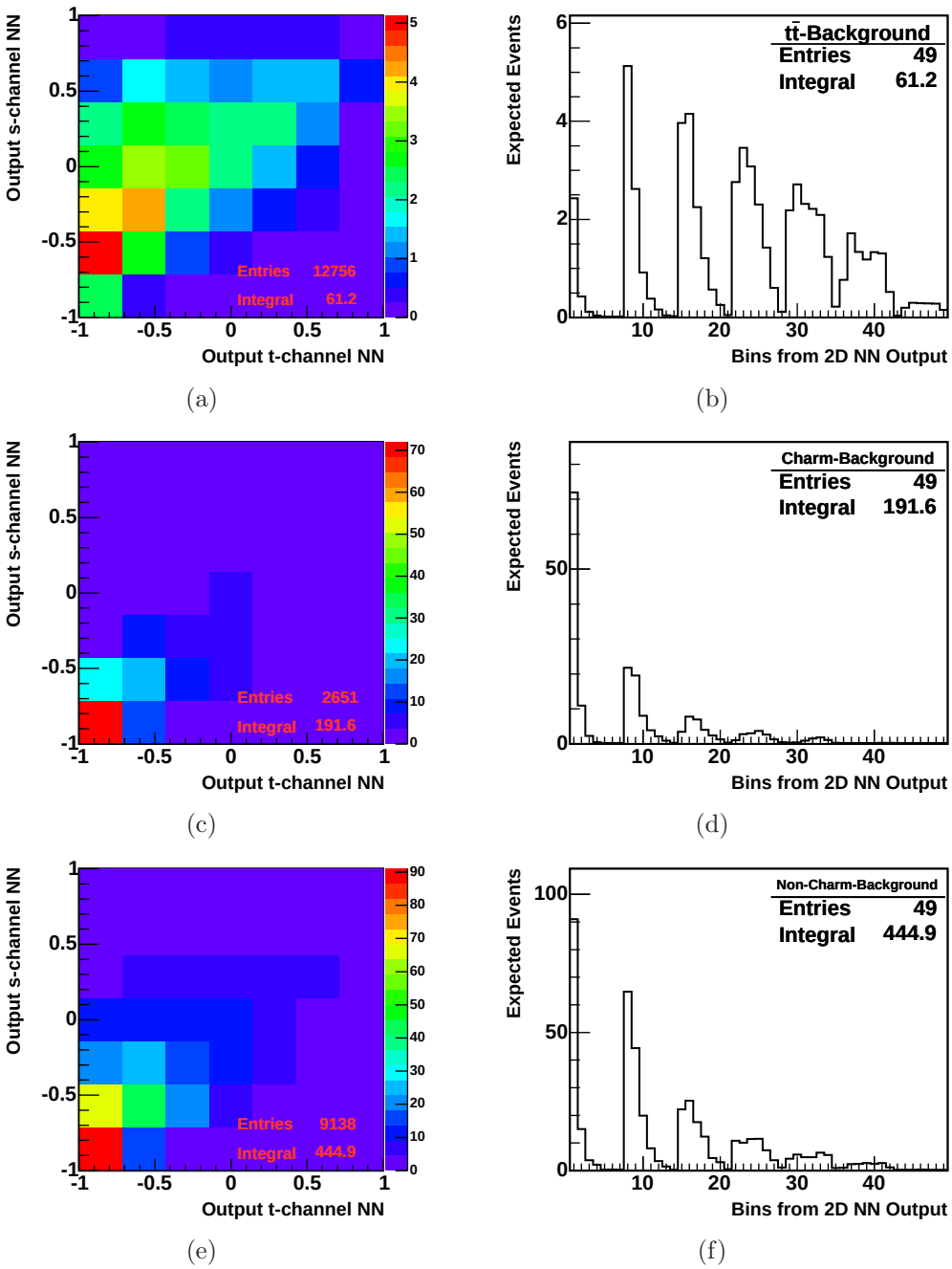

Figure 6.8: 2-jet-bin 2D NN Output (left hand side) and 1D template (right hand side) of the background samples: $t\bar{t}$ background (a) and (b), charm background (c) and (d) and non-charm background (e) and (f).

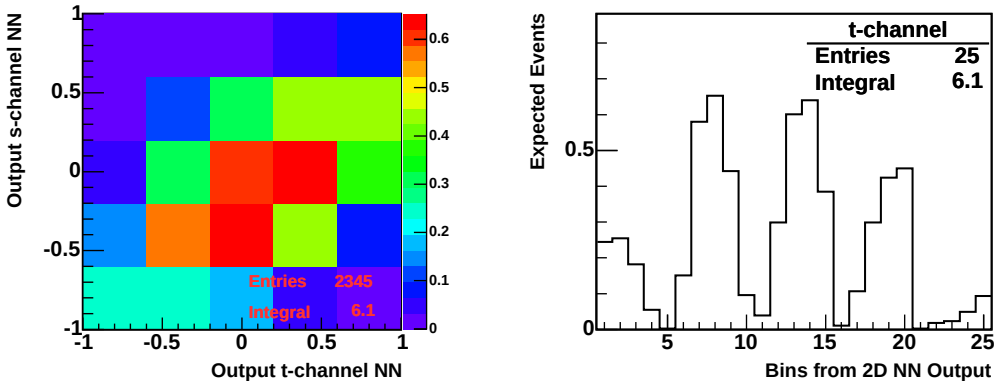

(a) (b)

Figure 6.9: 3-jet-bin 2D NN Output (a) and 1D template (b) of t-channel.

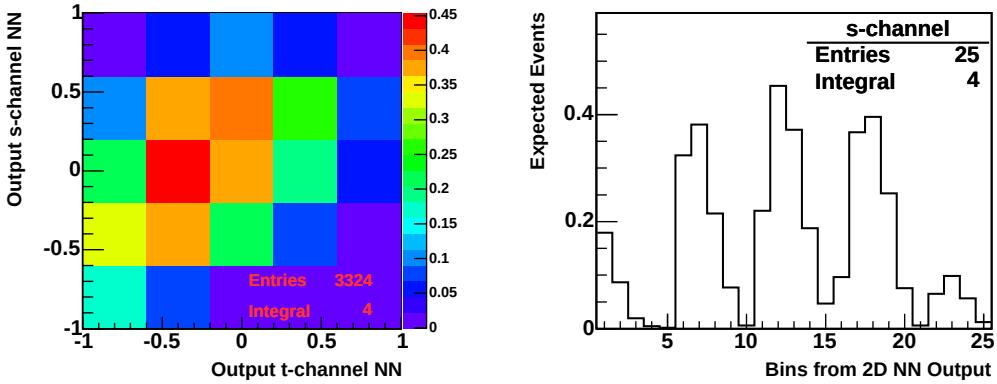

(a) (b)

Figure 6.10: 3-jet-bin 2D NN Output (a) and 1D template (b) of s-channel.

Figure 6.9 (a) and 6.10 (a) depict the 2D NN output for both signal samples in the 3-jet-bin. It is obvious, that the discrimination ability of the networks is not as good as in the 2-jet-bin.
The NN outputs for the background samples are seen in Figure 6.11. Again, the networks achieve to recognize the background-likeness of the events, even if some entries fluctuate into the signal regions of the output distributions.

It is important to emphasize that the shapes of all 1D templates differ from each other. This is fundamental for the fit of the Likelihood function to find the corresponding fractions of the different samples.

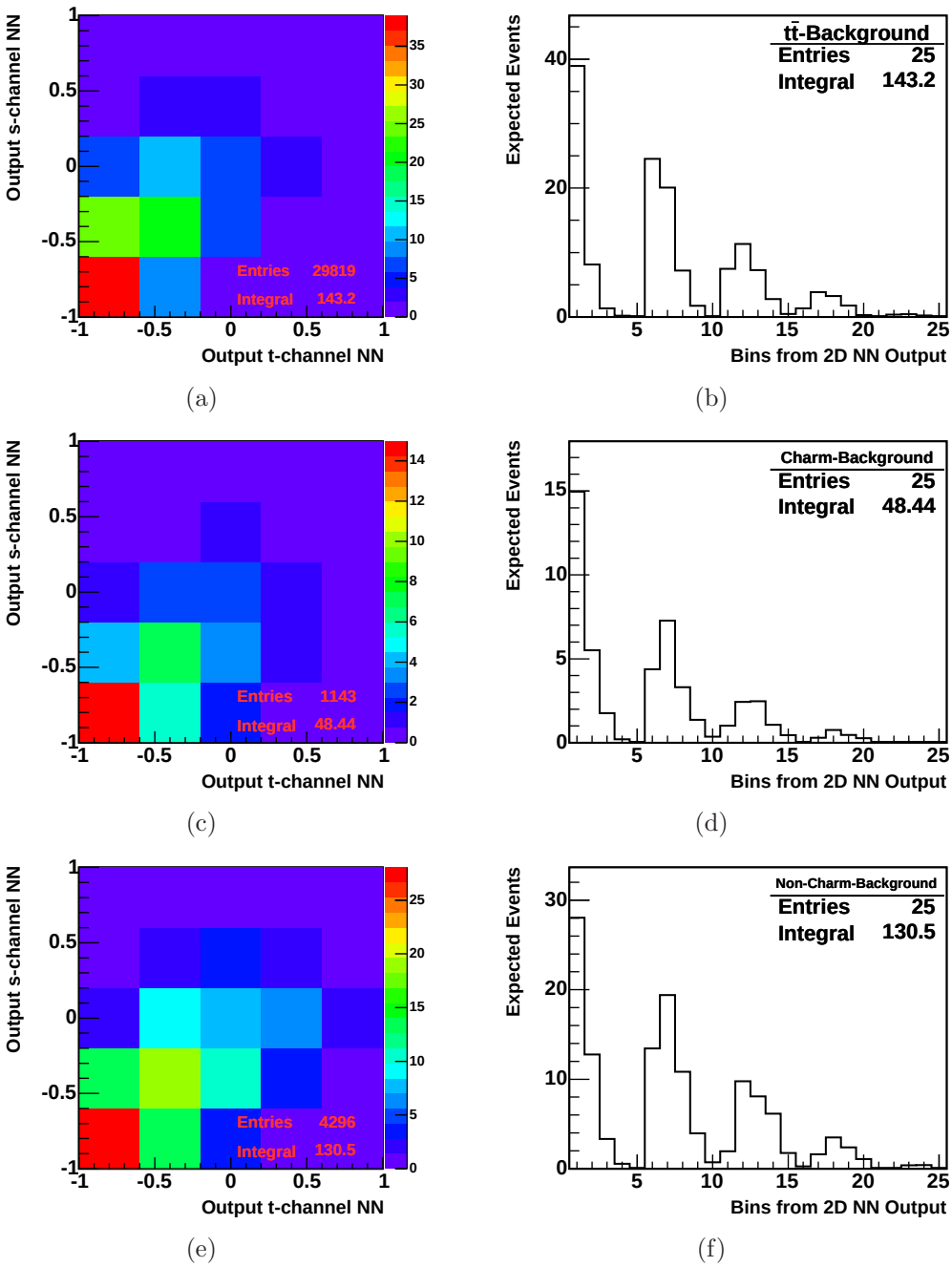

Figure 6.11: 3-jet-bin 2D NN Output (left hand side) and 1D template (right hand side) of the background samples: $t\bar{t}$ background (a) and (b), charm background (c) and (d) and non-charm background (e) and (f).

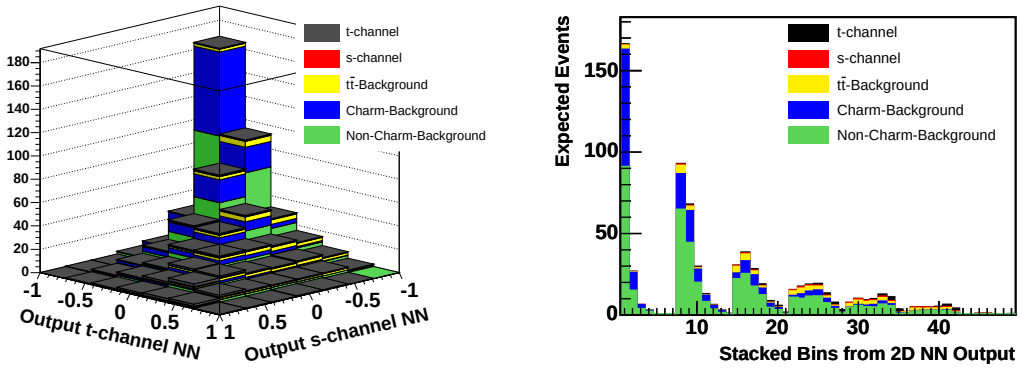

(a) (b)

Figure 6.12: Stacked 2-jet-bin 2D NN Output (a) and stacked 1D templates (b) of all samples.

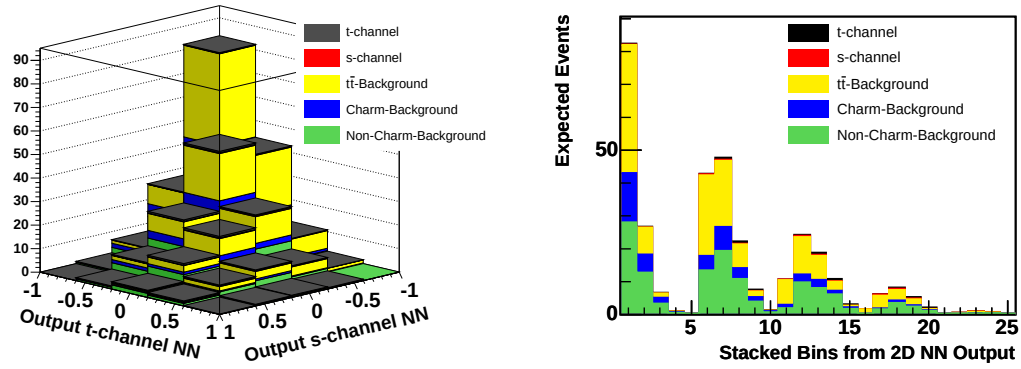

(a) (b)

Figure 6.13: Stacked 3-jet-bin 2D NN Output (a) and stacked 1D templates (b) of all samples.

The stacked distributions of all 2D and 1D NN output histograms are shown in Figure 6.12 and 6.13 for the 2-jet- and 3-jet-bin, respectively. In both subsamples, the s- and t-channel fractions are tiny. In the 2-jet-bin, the non-charm (particularly $Wb\bar{b}$ and mistags) background is dominating, whereas in the 3-jet-bin the $t\bar{t}$ and non-charm (again $Wb\bar{b}$ and mistags) backgrounds are prominent.

6.4 Simultaneous Likelihood-Fit of the Single-Top Cross Sections

In order to extract the s- and t-channel signal content of each pseudo data sample, a binned likelihood function, based on reference [40], is used. Likelihood functions are based on a known or estimated probability density function $f(x|a)$ where x is an observable and a is a set of unknown parameters to be estimated. The likelihood function $L(a)$ for a set of measured observables $x_1, x_2, \ldots x_n$ is defined by

$$L(a) = f(x_1|a) \cdot f(x_2|a) \cdots f(x_n|a) = \prod_{i=1}^{n} f(x_i|a) \tag{6.7}$$

This function $L(a)$ can be interpreted as the probability of obtaining the measured values x_i for a given parameter set a. So the best estimator $\hat{a}$ for the parameter set a is the one that maximizes the likelihood function $L(a)$ with respect to the given data set $\{x_i\}$.
Since a binned likelihood function is used for this study, the contents n_i of a set of bins i derived from a distribution are used as observables. The parameter a aimed to measure is the production cross section σ. For convenience reasons the parameter $\beta = \sigma/\sigma^{SM}$ is used, which is the cross section normalized to its Standard Model prediction.
The statistical content n_i of a bin i is described by the Poisson distribution

$$P(n_i) = \frac{\mu_i^{n_i}}{n_i!} e^{-\mu_i} \tag{6.8}$$

where μ_i denotes the expectation value of the distribution in this bin i. This expectation value μ_i is the sum of all signal and background process expectation values μ_{ji} contributing to the specific bin i. Each μ_{ji} is the product of the normalized production cross section β_j times a bin specific acceptance function ν_{ji}. Thus the Poisson mean for a bin i in the presence of d signal and background processes is

$$\mu_i = \sum_{j=1}^{d} \mu_{ji} = \sum_{j=1}^{d} \nu_{ji}\beta_j. \tag{6.9}$$

The likelihood consisting of q bins within this scenario is defined by

$$L(\beta) = \prod_{i=1}^{q} \frac{\mu_i^{n_i}}{n_i!} e^{-\mu_i}. \tag{6.10}$$

As discussed, the pseudo data sample is divided in two subsamples (2-jet- and 3-jet-bin) defined by the number of jets in the event. Five classes of processes are considered: The s- and t-channel single-top production modes, $t\bar{t}$ background, charm background and non-charm background. In addition, the background contributions are constrained by Gaussian functions $G(\beta_j, 1.0, \Delta_j)$ of variable β_j with mean 1.0 and standard deviation Δ_j.

Due to practical reasons the acceptance function ν_{ji} given in equation (6.9) is divided in two parts:

$$\nu_{ji} = \nu_j \alpha_{ji}, \tag{6.11}$$

Here, the term ν_j reflects the absolute acceptance of process j, which is the event detection efficiency multiplied with the integrated luminosity (see Chapter 6.1). α_{ji} denotes the relative acceptance within bin i, given by the normalized content of bin i of the template histogram for process j.
Thus, the likelihood function L equals:

$$\begin{aligned} L &= L(\beta_{s-ch}, \beta_{t-ch}, \beta_{t\bar{t}}, \beta_{charm}, \beta_{non-charm}) \\ &= L(\beta_1, \dots, \beta_5) \\ &= \prod_{i=1}^{B_2} \frac{e^{-\mu_i} \cdot \mu_i^{n_i}}{n_i!} \cdot \prod_{j=1}^{B_3} \frac{e^{-\mu_j} \cdot \mu_j^{n_j}}{n_j!} \cdot \prod_{k=3}^{5} G(\beta_k, 1.0, \Delta_k) \end{aligned} \tag{6.12}$$

The first factors are Poisson terms for the bins of the 2-jet-bin template (index i) and 3-jet-bin template (index j). The third factor is the Gaussian integration kernel of the backgrounds which constrain the nuisance parameters to the expectation.
The expected mean in bin i is:

$$\mu_i = \sum_{k=1}^{5} \beta_k \cdot \nu_k \cdot \alpha_{ki} \tag{6.13}$$

To obtain the probability distribution for the SM normalized signal cross sections β_{s-ch} and β_{t-ch}, we integrate out all nuisance parameters from the likelihood function:

$$L^*(\beta_{s-ch}, \beta_{t-ch}) = \int_0^{+\infty} \int_0^{+\infty} \int_0^{+\infty} L(\beta_1, \dots, \beta_5)\, d\beta_3 d\beta_4 d\beta_5 \tag{6.14}$$

This reduced or marginalized likelihood only depends on the normalized signal cross sections. The integration is implemented as a Monte Carlo integration. For each Monte Carlo integration point random numbers are generated for the nuisance parameters β_k according to Gaussian distributions $G(\beta_k, 1.0, \Delta_k)$. Based on reference [38] we choose $\Delta_3 = 23\%$ for the $t\bar{t}$ background and $\Delta_4 = \Delta_5 = 20\%$ for the charm and non-charm background. The marginalized likelihood is finally maximized with respect to the pseudo data set.

The distributions of the randomly generated numbers of pseudo events for each process are shown in Figure 6.15 - 6.19. The sum of these numbers for each pseudo experiment is the number of events in the pseudo data set. Its distribution for 10000 pseudo experiments can be seen in Figure 6.14. All shown distributions have their mean very close to the number of SM predicted events for the given integrated luminosity of 1 fb^{-1}, as required.

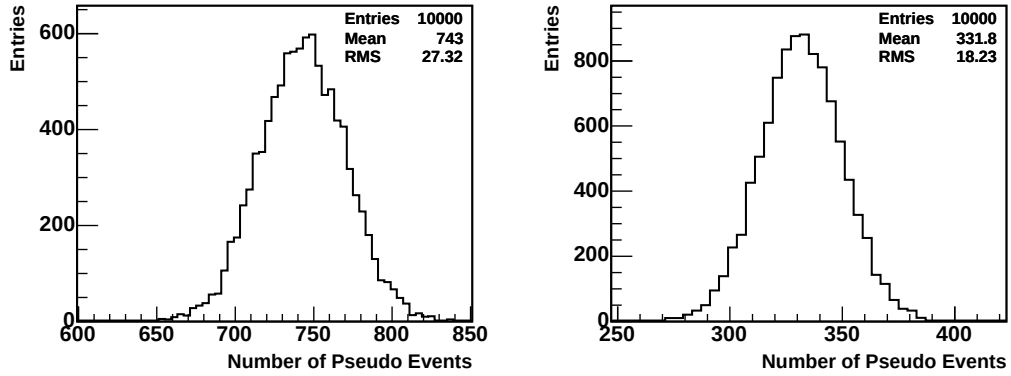

(a) (b)

Figure 6.14: Distribution of generated pseudo events for data in the 2-jet- (a) and 3-jet-bin (b). By Standard Model prediction 743.3 and 332.3 events are expected.

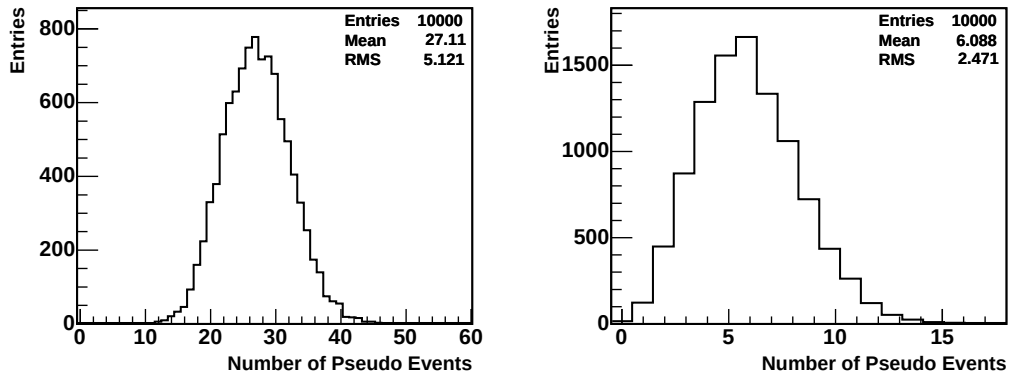

(a) (b)

Figure 6.15: Distribution of generated pseudo events for t-channel signal in the 2-jet- (a) and 3-jet-bin (b). By Standard Model prediction 27.2 and 6.1 events are expected.

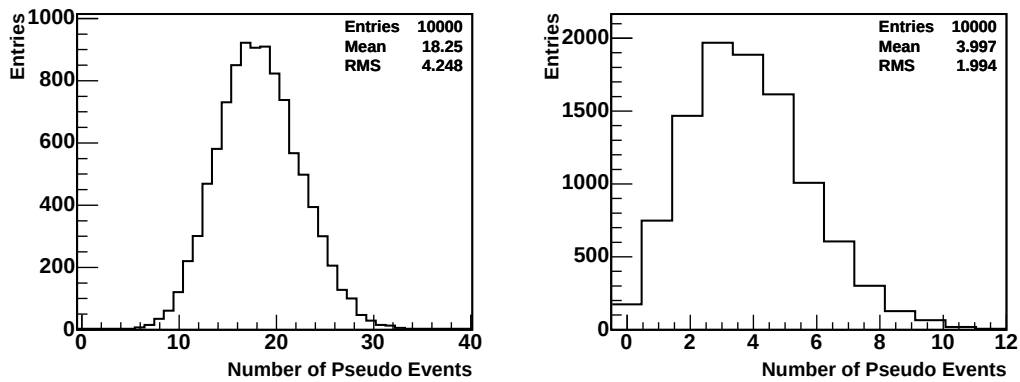

(a) (b)

Figure 6.16: Distribution of generated pseudo events for s-channel signal in the 2-jet- (a) and 3-jet-bin (b). By Standard Model prediction 18.4 and 4.0 events are expected.

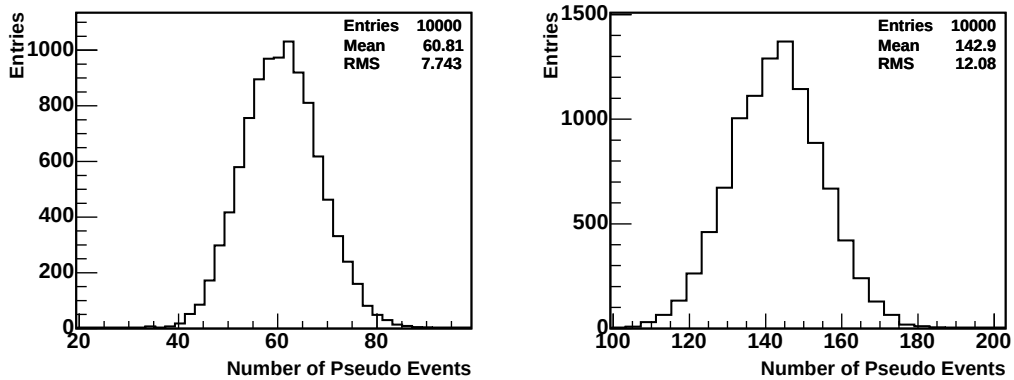

(a) (b)

Figure 6.17: Distribution of generated pseudo events for $t\bar{t}$ background in the 2-jet- (a) and 3-jet-bin (b). By Standard Model prediction 61.2 and 143.2 events are expected.

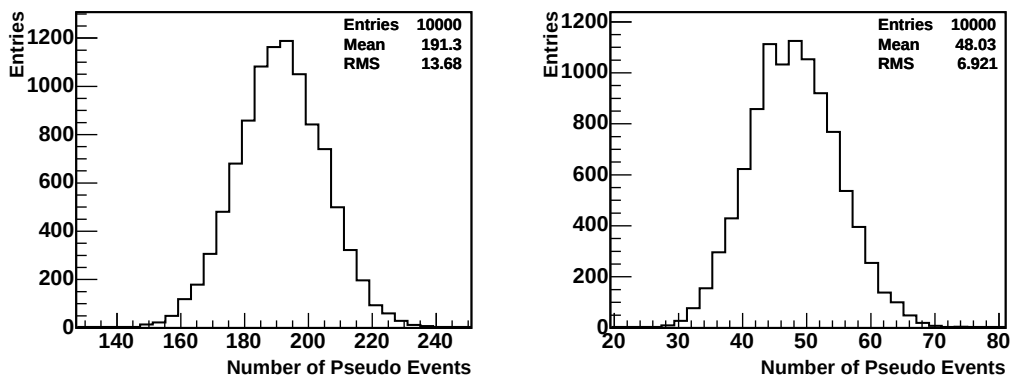

(a) (b)

Figure 6.18: Distribution of generated pseudo events for charm background in the 2-jet- (a) and 3-jet-bin (b). By Standard Model prediction 191.6 and 48.4 events are expected.

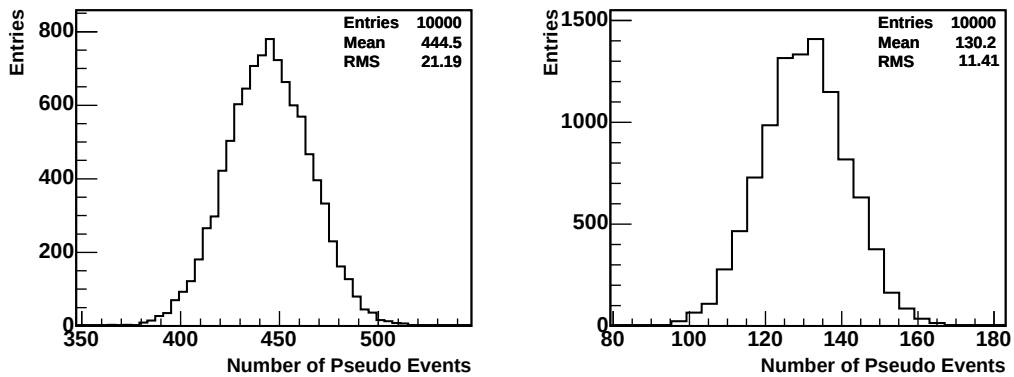

(a) (b)

Figure 6.19: Distribution of generated pseudo events for non-charm background in the 2-jet- (a) and 3-jet-bin (b). By Standard Model prediction 444.9 and 130.5 events are expected.

The estimates of the likelihood fits for the Standard Model normalized s- and t-channel cross sections β_{s-ch} and β_{t-ch} are shown in Figure 6.20 (a) and (b), respectively. It is obvious, that the distribution of the t-channel estimates from the 10000 pseudo experiments is clearly more narrow compared to the s-channel, also the mean is very close to the SM expected value of 1.0, whereas the s-channel has a mean of about 1.3. The distributions of β_{s-ch} and β_{t-ch} are both approximately Gaussian in shape.
The s-channel distribution has about 10% of its entries in the zero-bin, i.e. in 10% of the pseudo experiments the likelihood fit could not indicate an s-channel contribution to the total number of pseudo events. These entries in the zero-bin force the mean to a higher value than 1.0. However, the median of the distribution of about 1.25 indicates, that for the s-channel the probability to measure a higher cross section than the one predicted by the Standard Model is enhanced. A reason for this could be the less discrimination ability of the s-channel neural net.

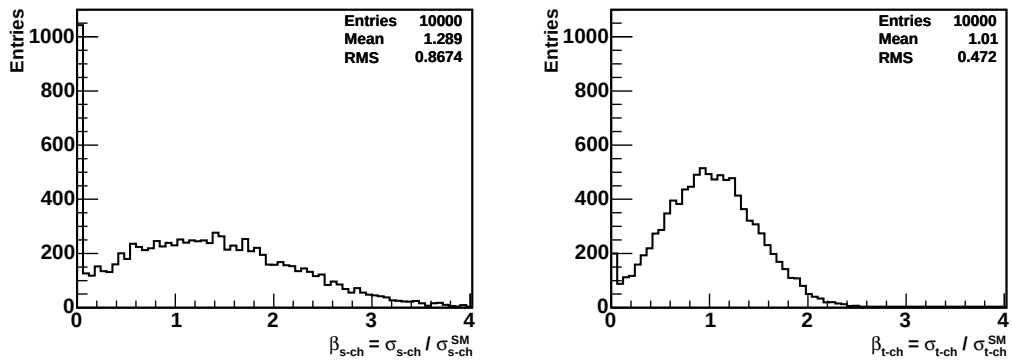

(a) (b)

Figure 6.20: Pseudo experiment distribution of s-channel (a) and t-channel (b) cross section measurement normalized to the SM prediction for an integrated luminosity of 1 fb^{-1}.

The statistical uncertainties for both measurements are given by the root-mean-squared (RMS) values of the corresponding distributions. Through this, the entries in the zero-bins are taken into account. This would not be the case by choosing the standard deviation parameter of a Gaussian fit to the distributions, although the differences are minor. As already mentioned, systematic uncertainties are not included in this study.

Presuming a Standard Model single-top production, we would expect to obtain an s-channel cross section measurement with a statistical uncertainty of about $\pm 89\%$ corresponding to $\sigma_{s-ch} = 0.88 \pm 0.78$ pb. For the t-channel production mode, a measurement with a statistical uncertainty of about $\pm 47\%$ could be expected, which would correspond to a cross section of $\sigma_{t-ch} = 1.98 \pm 0.93$ pb.

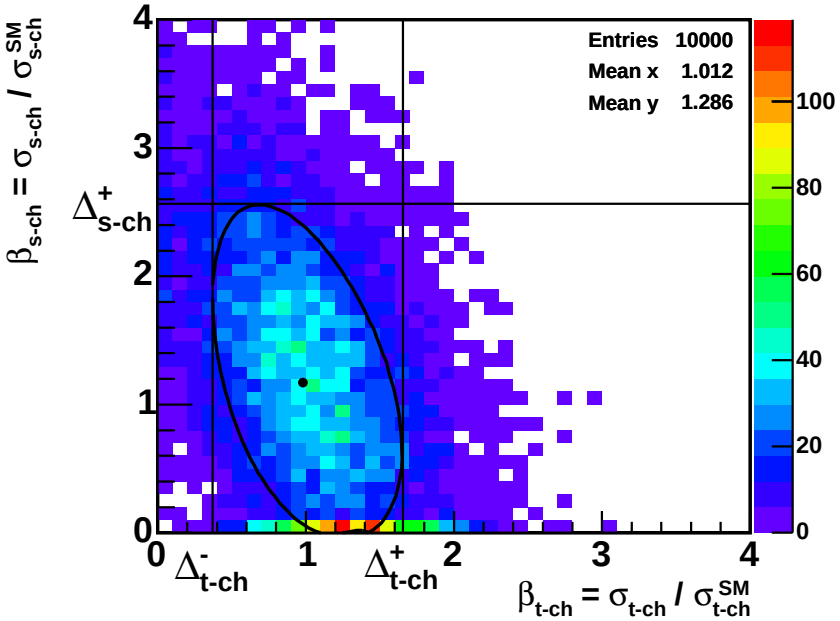

Figure 6.21: Pseudo experiment 2D-distribution of t- vs. s-channel cross section measurement normalized to the SM predictions for an integrated luminosity of 1 fb^{-1}. In addition, the $1\sigma_{stat}$ contour of the fit estimate of a selected individual pseudo experiment with $\beta_{t-ch} = 0.98$ and $\beta_{s-ch} = 1.17$ is included. The tangents to the contour correspond to $\Delta^{\pm} = \beta \pm \sigma_{stat}$.

Figure 6.21 depicts the distribution of t- vs. s-channel cross section measurement for all pseudo experiments. The fact that the entries in the 2D plot are tilted shows that β_{s-ch} and β_{t-ch} are correlated, strictly speaking negative correlated. Consequently, if one found a value of $\beta_{t-ch} > 1.0$, this would lead to an enhanced probability to find a value of $\beta_{s-ch} < 1.0$ and vice versa.

It is clearly visible, that the entries of the s-channel zero-bin ($\beta_{s-ch} = 0$) accumulate at higher values of β_{t-ch}, their mean is about 1.3. In those pseudo events the likelihood fit is not able to find an appropriate s-channel signal and thus the t-channel fraction has a higher probability to increase. The same is valid for the $\beta_{t-ch} = 0$ values, although the fraction is much smaller. Their mean value of β_{s-ch} is about 2.3.

Additionally, Figure 6.21 shows the likelihood fit estimate of one selected pseudo experiment out of the total of 10000. The marker at $(\beta_{t-ch}|\beta_{s-ch}) = (0.98|1.17)$ points out the best likelihood fit value for both signal cross sections of this individual pseudo data set. The elliptic figure depicts the $1\sigma_{stat}$ contour calculated by the likelihood fit. Its tangents correspond to $\beta \pm \sigma_{stat}$. For this selected example we would obtain estimated s- and t-channel statistical uncertainties of about $\sigma^{s-ch}_{stat} = {}^{+136\%}_{-126\%}$ and $\sigma^{t-ch}_{stat} = {}^{+35\%}_{-31\%}$ and therefore estimated single-top cross sections of about $\sigma_{s-ch} = 1.03\ {}^{+1.40}_{-1.30}$ pb and $\sigma_{t-ch} = 1.94\ {}^{+0.68}_{-0.61}$ pb, respectively.

Chapter 7

Conclusions and Outlook

In this thesis, the t-channel matching procedure of two single-top signal Monte Carlo samples is optimized. The s- and matched t-channel samples, generated by MadEvent, are validated by comparing to ZTOP next-to-leading-order calculations. We find good agreement for all kinematic distributions we investigate, except for softer light quark jets due to gluon radiation. Since this has only minor impact on the s-channel, the corresponding MadEvent sample performs its task as expected. For the t-channel, we can conclude that the applied matching procedure leads to a MadEvent sample that successfully describes the kinematic distributions and rates of the 2nd-b quark. However, small differences remain. The discrepancy in the p_T-ordered 2nd-leading light jets is mainly due to the absence of initial state gluon splitting and initial and final state gluon radiation matrix elements in the MadEvent sample production. The subsequent PYTHIA showering of the partons is apparently inappropriate for modeling those contributions and not intended for this purpose.
The proper way would be to produce all relevant NLO matrix elements and match them as proposed in reference [15]. At present, an NLO-MC-generator for single-top is in preparation [41]. Probably it will be available for future iterations of single-top analyses and will redundantize further matching procedures.
We estimate the systematic uncertainty on the single-top acceptance due to the Monte Carlo modeling and find an uncertainty of about 1% on the t-channel acceptance. We obtain a negligible uncertainty well below 1% on the s-channel acceptance. These acceptance uncertainties are very well acceptable for the single-top analyses that are currently under way.
A sensitivity study of the simultaneous cross section measurement of the s- and t-channel single-top production modes is conducted. For this purpose, only statistical uncertainties are included. For a future integrated luminosity of 1 fb^{-1}, we expect to obtain an s-channel cross section measurement with a statistical uncertainty of about $\pm 89\%$. For the t-channel, the study predicts a measurement with a statistical uncertainty of about $\pm 47\%$.
This study is a first look at a new method, further developments are mandatory. The latest single-top and background MC samples and the corresponding systematic uncertainties have to be included. In addition, final trainings of the neural nets should be available to obtain a reliable sensitivity of the cross section measurements.

Bibliography

[1] CDF Collaboration, F. Abe *et al.*, Phys. Rev. Lett. **74**, 2626 (1995).

[2] DØ Collaboration, S. Abachi *et al.*, Phys. Rev. Lett. **74**, 2632 (1995).

[3] CDF Collaboration, D. Acosta *et al.*, Phys. Rev. D **65**, 091102 (2002).

[4] CDF Collaboration, D. Acosta *et al.*, Phys. Rev. D **69**, 052003 (2004).

[5] DØ Collaboration, V. M. Abazov *et al.*, Phys. Rev. Lett. B **517**, 282 (2001).

[6] DØ Collaboration, B. Abbott *et al.*, Phys. Rev. D **63**, 031101 (2001).

[7] CDF Collaboration, D. Acosta *et al.*, Phys. Rev. D **71**, 012005 (2005).

[8] DØ Collaboration, V. M. Abazov *et al.*, Phys. Rev. Lett. B **622**, 265 (2005).

[9] W. Wagner, Rep. Prog. Phys. **68**, 2409 (2005).

[10] T. Sjöstrand *et al.*, Comp. Phys. Commun. **135**, 238 (2001).

[11] E. E. Boos, L. V. Dudko and V. I. Savrin, CMS Note 2000/065 (2000).

[12] T. Stelzer and W. F. Long, Comp. Phys. Commun. **81**, 357 (1994).

[13] F. Maltoni and T. Stelzer, hep-ph/0208156 (2002).

[14] C. Ciobanu *et al.*, CDF Note 7020 (2004).

[15] Z. Sullivan, Phys. Rev. D **70**, 114012 (2004).

[16] Th. Müller, 'Die Suche nach den Fundamentalen Bausteinen der Natur',
Talk at the 'Physik am Samstag'-lecture series in Karlsruhe, Germany (2003).

[17] J. L. Tonry *et al.*, Astrophys. J. **594**, 1 (2003).

[18] C. L. Bennett *et al.*, Astrophys. J. Suppl. **148** 1 (2003).

[19] S. Eidelman *et al.*, Phys. Rev. Lett. B **592**, 1 (2004)
and 2005 partial update for the 2006 edition available on http://pdg.lbl.gov/

[20] H. L. Lai *et al.*, Eur. Phys. J. C **12**, 375 (2000).

[21] N. Cabbibo, Phys. Rev. Lett. **10**, 531 (1963).

[22] M. Kobayashi and T. Maskawa, Prog. Theor. Phys. **49**, 652 (1973).

[23] N. Kidonakis and R. Vogt, Phys. Rev. D **68**, 114014 (2003).

[24] M. Cacciari *et al.*, J. High Energy Phys. **0404**, 068 (2004).

[25] B. W. Harris *et al.*, Phys. Rev. D **66**, 054024 (2002).

[26] T. M. P. Tait, Phys. Rev. D **61**, 034001 (2000).

[27] D. O. Carlson and C. P. Yuan, Phys. Lett. B **306**, 386 (1993).

[28] G. Mahlon and S. Parke, Phys. Rev. D **55**, 7249 (1997).

[29] A. P. Heinson, A. S. Belyaev and E. E. Boos, Phys. Rev. D **56**, 3114 (1997).

[30] T. Stelzer, Z. Sullivan and S. Willenbrock, Phys. Rev. D **56**, 5919 (1997).

[31] CDF Collaboration, R. Blair *et al.*, FERMILAB-Pub-96/390-E (1996).

[32] R. Brun and F. Carminati, CERN Programming Library Long Writeup **W5013** (1993).

[33] E. Gerchtein and M. Paulini, physics/0306031 (2003).

[34] V. N. Gribov and L. N. Lipatov, Yad. Fiz. **15**, 781 (1972).

[35] G. Altarelli and G. Parisi, Nucl. Phys. B **126**, 298 (1977).

[36] Y. L. Dokshitzer, Sov. Phys. JETP **46**, 641 (1977).

[37] R. Erbacher *et al.*, CDF Note 7372 (2004).

[38] S. Budd *et al.*, CDF Note 7863 (2005).

[39] M. Feindt, e-Print Archive physics/0402093 (2004).

[40] C. Ciobanu *et al.*, CDF Note 7106 (2004).

[41] S. Frixione *et al.*, hep-ph/0512250 (2005).